Low-Cost Hinge for Deployable Structures

S. Pellegrino, E. Kebadze, T. Lefort,
and A.M. Watt

CUED/D-STRUCT/TR202

ASTRIUM Study Manager: Mark Roe
Contract no. 24070108

Release date: 10 July 2002

Summary

This report presents a study of a recently proposed low-cost hinge for deployable spacecraft appendages. The hinge consists of one or more pairs of steel carpenter tapes (tape springs) connected to a rolling hinge made from plastic "wheels" connected by steel cables (Rolamite). This hinge is known as Tape-Spring Rolamite (TSR) hinge.

The report includes: a brief review of the relevant background to TSR hinges; a study of the moment-rotation relationship of TSR hinges; parametric relationships between key values of the moment-rotation relationship in terms of key design parameters, leading to the design of an improved hinge that is better suited for most practical applications; an extensive experimental study of the stiffness of a TSR hinge in the deployed state, backed by simple analytical predictions that are shown to be reasonably accurate for design purposes; analytical stiffness predictions in the deployed configuration; and deployment experiments on lightweight sandwich panels connected by TSR hinges, with an assessment of the performance of different damping mechanisms.

The key achievements of this study are: (i) experimental stiffness data for TSR hinges, (ii) experimentally validated analytical methods for predicting stiffness; (iii) detailed finite-element simulations of the folding/unfolding process; (iv) improved hinge design; and (v) assessment of passive damping methods for reducing end shock.

Contents

Chapter 1

Introduction

A new low-cost hinge for deployable appendages was recently proposed by Pellegrino et al. (2000). The hinge consists of one or more pairs of steel carpenter tapes —referred to as *tape springs* in this report— connected to a rolling hinge —referred to as *Rolamite hinge*— made from plastic "wheels" connected by steel cables. This hinge is known as Tape-Spring Rolamite (TSR) hinge, and a full description of its concept can be found in Pellegrino et al. (2000).

The main aim of the research presented in this report was to advance the proposed hinge beyond the concept stage, by

- investigating its performance in greater detail, both computationally and experimentally;
- exploring the sensitivity of the hinge response to changes in its design parameters;
- constructing good quality hardware models, and testing them;
- investigating damping mechanisms that could be used to reduce the shock transmitted by the hinge to the spacecraft.

The new low-cost hinge has been proposed as the deployment mechanism for a number of deployable systems on satellites, including deployable radiators, synthetic aperture radars (SARs) and solar panels among others. In designing such systems there are two main properties of the hinges that are of particular interest:

- Stiffness. The stiffness of the hinges has to be found in order to determine the natural frequency of the deployed structures and the maximum launch forces imposed on the structure.
- Moment-Rotation profile. The deployment dynamics of the structure will have to be predicted in order to ensure correct deployment in a controlled manner without damage occurring to the constituent parts. This will require knowledge of the moment developed by the hinge with respect to the rotation.

1.1 Description of Hinge

Figure 1.1 is an overall view of a TSR hinge (actually, version 1, see below), shown both fully deployed and fully folded. Detailed drawings are shown in Appendix A, but the main geometric characteristics of these hinges are defined in Figures 1.2 and 1.3.

There are in general five design parameters, as follows:

- the total length L of the tape springs;
- the separation distance s between the tape springs, i.e. the distance from the bottom of the lower tape to the top of the upper tape;
- the offset d between the centre line through the two tape springs and the line through the centres of the Rolamite wheels.
- the radius of the Rolamite wheels, r.
- the radius of curvature of the tape-spring, R_c. This is, however, fixed if off-the-shelf tape-springs are used.

In order to reduce the size of the design envelope the following constraints were introduced

$$s - d < r \tag{1.1}$$

$$L > 2\pi R_c \tag{1.2}$$

$$d > s/2 \tag{1.3}$$

Equation 1.1 arises from the fact that the hinge is required to fold 180° without the two sides clashing. Equation 1.2 arises from the fact that the length of the straight tape-spring must be longer than the perimeter of the half circle described by the hinge in the folded position. This is assuming that the tape-spring folds into an arc of constant radius, R_c, which is true for a tape-spring subjected solely to end-moments (Seffen and Pellegrino, 1999); however note that in the present case contact between the two tape springs will change somewhat the loading to which the springs are subjected.

Finally, Equation 1.3 is required to avoid that at least one of the tape-springs be subjected to large tensile stresses for rotations of about 180°.

The Rolamite wheels are manufactured from Delrin (a space-qualified Acetyl Resin), Aluminium-alloy blocks connect the rolling bodies and tape-springs together. Prestressed stainless steel wire is used to hold together the wheels and is terminated by crimped aluminium tubes, with tension adjustment provided at one end by the wire passing through a screw with a lock-nut on the end. The tape-springs are cut from a "Contractor Grade" steel tape-measure ($R_c =$ 15 mm), supplied by Sears Roebuck and Co.

Two hinge configurations are of particular interest in this report; version 1 has $d = 4.5$ mm and version 2 has $d = 11$ mm. All other parameters have the same values for both hinges, which are $s = 16$ mm, $r = 28.1$ mm, and $L = 126$ mm; see Table 1.1.

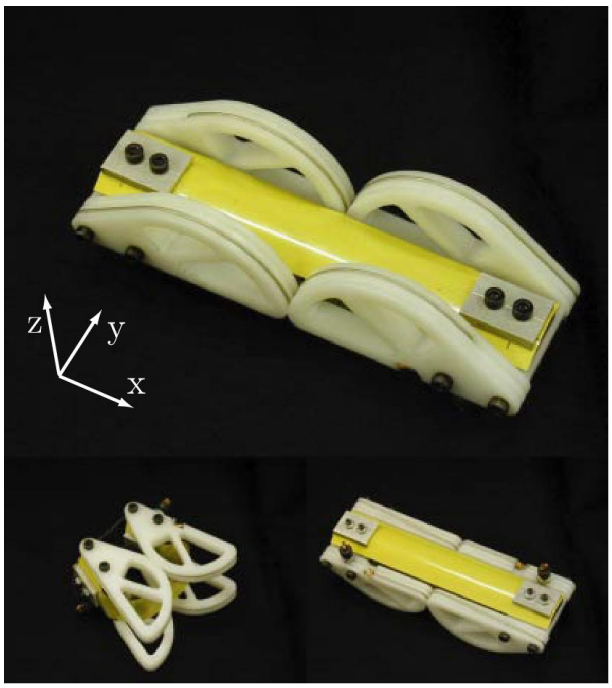

Figure 1.1: TSR hinge.

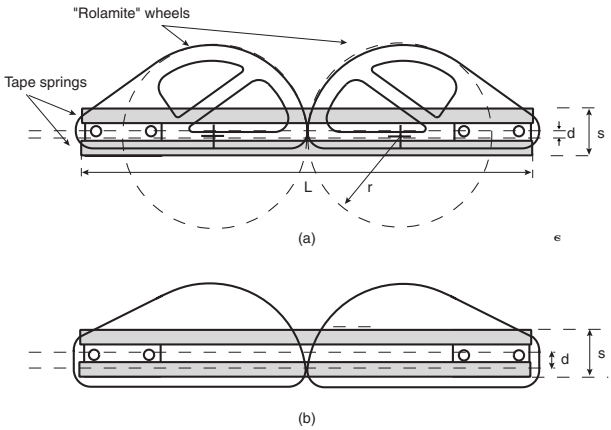

Figure 1.2: TSR Hinge, (a) Version 1 ($d = 4.5$ mm); (b) Version 2 ($d = 11$ mm).

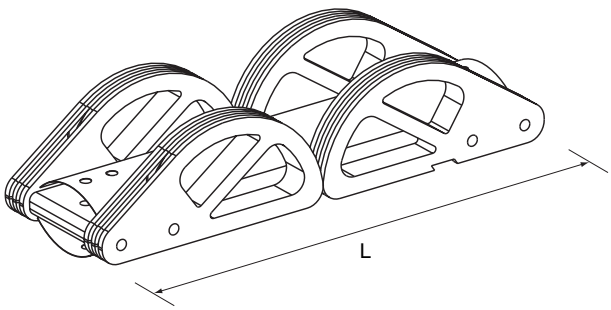

Figure 1.3: TSR hinge.

	Version 1	Version 2
Tape-spring length, L	126	126
Tape-spring separation, s	16	16
Offset, d	4.5	11
Radius of Rolamite, r	28.1	28.1
Tape-spring radius, R_c	15	15

Table 1.1: Parameters of TSR hinges (mm).

1.2 Layout of this Report

This report consists of 8 chapters, as follows.

Following the present, introductory chapter, Chapter 2 reviews the relevant background to TSR hinges and, in particular, traces the history of patents on tape springs and Rolamite hinges. Damping methods are briefly reviewed.

Chapter 3 investigates the moment-rotation relationship of TSR hinges, both experimentally and computationally. An important difference in behaviour between the version 1 and version 2 hinges is identified.

Chapter 4 presents a parametric study of the moment-rotation relationship of TSR hinges in terms of their key design parameters. The conclusion from this study is that the version 2 hinge is better suited for most practical applications and could be further improved.

Chapter 5 presents an extensive experimental study of the stiffness of the version 1 hinge in the deployed state, and also develops simple analytical predictive methods that are shown to be reasonably accurate for design purposes. The separate contributions of the tape springs and Rolamite elements to the total stiffness of the hinge are characterized.

Chapter 6 presents analytical predictions of the stiffness of TSR hinges (identical for versions 1 and 2).

Chapter 7 presents a set of deployment experiments on lightweight sandwich panels connected by two TSR hinges version 2; several damping mechanisms are investigated. A deployment simulation is also presented; this is based on an ABAQUS simulation of the moment-rotation relationship of the hinges, incorporated in the overall deployment behaviour of the panels, with Pro/Mechanica Motion. Detailed measurements of shock behind the hinge attachments are presented, and alternative damping methods that were considered at an earlier stage of the study are briefly outlined.

Chapter 8 concludes the report.

Chapter 2

Background

Simple self-actuating, self-locking hinges have been developed for a number of years for use as the deploying mechanisms for solar cells, synthetic aperture radars (SARs), booms, radiators and the like. One successful design is the use of tape-spring hinges, see Chironis and Sclater (1996) for example.

2.1 Tape-Spring Hinges

The use of curved elastic elements (such as tape-springs) to produce low-friction locking hinges has a long provenance within the space industry. Tape-spring hinges offer a number of benefits over a standard pin-jointed hinge that make them particularly suitable for use in deployable space structures:

- Elastically latch into locked position giving highly repeatable and accurate positioning.
- No moving parts to jam or bind due to long-term storage or adverse environmental conditions.
- Simple manufacture.

In order to improve the locking function of these hinges the curved elastic elements have been offset from each other in order to place them in tension and compression rather than in bending. Such a scheme for arranging curved elements was patented by Vyvyan (1968) and can be seen in the deployed and folded states in Figure 2.1.

Alternate layouts of the tape springs are possible such as that shown in Figure 2.2 (Chiappetta et al., 1993). It should be noted that this patent is not making claims on the layout of the tape-springs but purely on the method of affixing the tape-springs to the rest of the structure.

2.2 Tape-spring Rolling Hinges

Although tape-spring hinges offer a number of advantages over standard pin-joint style hinges they provide no stiffness in the undeployed configuration. This

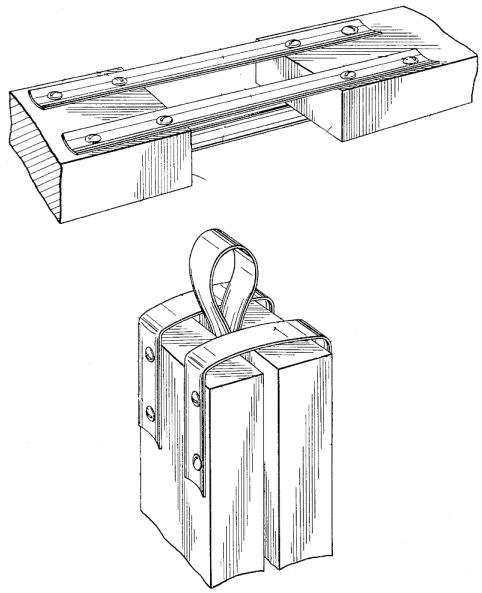

Figure 2.1: Hinge layout from (Vyvyan, 1968).

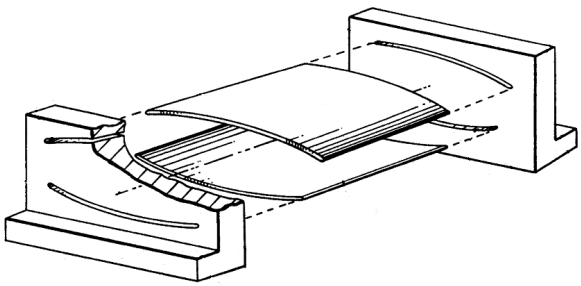

Figure 2.2: Hinge layout from Chiappetta et al. (1993).

can cause uncertainties in the deployment and makes gravity compensation in land-based testing problematic.

A solution to this problem has been proposed in Auternaud et al. (1992). A single tape-spring hinge is attached to a rolling (or Rolamite style) joint as shown in Figure 2.3.

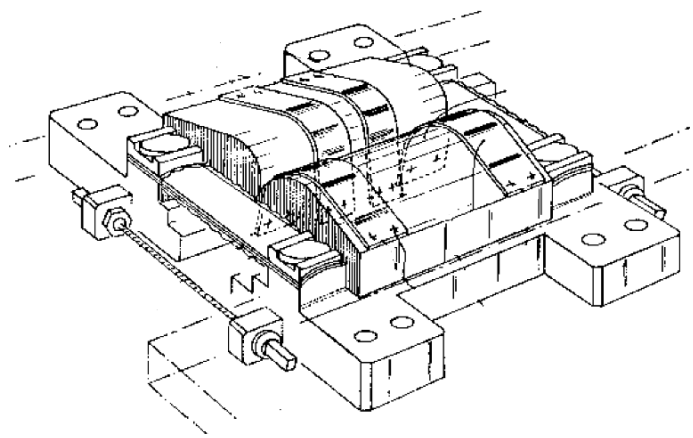

Figure 2.3: Tape-spring hinge with rolling joint (Auternaud et al., 1992).

The rolling joint controls the deployment kinematics of the tape-spring hinge, constraining it to rotate in one plane only. The rolling joint as shown in Hilberry and Hall (1976), shown in Figure 2.4, was developed from the linear roller-band device shown in Wilkes (1969) which can be seen in Figure 2.5. This is a linear bearing with rollers that are held in place by tensioned bands. Because there is no sliding within the joint, only rolling, friction is very low and there is no need for oils or other lubricating fluids. This attribute makes rolling joints well suited for use in a space environment.

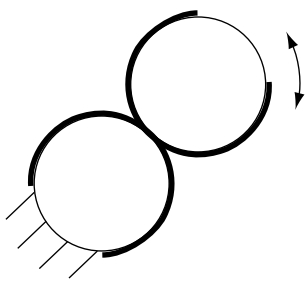

Figure 2.4: Rolling hinge.

Hilberry and Hall (1976) also describe how the performance of a rolling hinge can be modified by changing the profile of the rolling or tension band surfaces. By making the bands run in a smaller radius than the rolling surface, Figure 2.6, tension in the wire will pull the two halves of the hinge together. By modifying two of the four band surfaces to be smaller than the other two as shown in Figure 2.7 a moment is created on rotating the hinge.

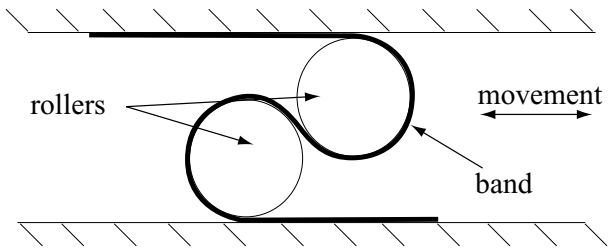

Figure 2.5: Linear roller-band device.

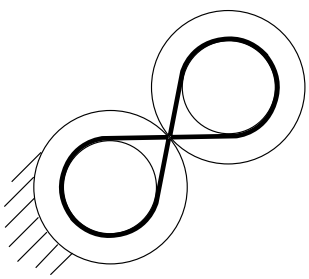

Figure 2.6: Rolling hinge tensioning the two halves.

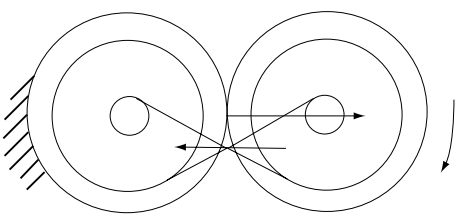

Figure 2.7: Rolling hinge that creates moment on rotation.

2.3 Damping of Hinges

On latching at the end of deployment there is often a large shock transmitted from the hinge to the spacecraft structure. There have been attempts to reduce this shock by use of damping within the hinge. Dupperray et al. (2001) describes the addition of a constrained damping layer to the tape-springs. On bending the tape-springs a damping material that is constrained between two surfaces is subjected to shear stress. The damping material resists this stress and slows down the motion of the hinge.

Chapter 3

Moment-Rotation Profile

The finite element package ABAQUS (Hibbit et al. 2001) was used to simulate the moment-rotation properties of TSR hinges. A numerical approach was required, as the analytical techniques developed by Seffen and Pellegrino (1999) are not suitable for analysing tape-springs in which contact between the tapes has significant effects. The results from ABAQUS were then compared to experimental results.

3.1 Finite Element Model

The purpose of this model was to capture the snap-through deformation and contact between the tape springs of a TSR hinge during folding/deployment and to extract the bending moment-rotation relationship. The model will also predict the maximum, i.e. buckling, moment that can be applied to a TSR hinge in its deployed configuration.

The model was built in such way that changing the variables, i.e. the parameters d, L and s, is as simple as possible.

Taking all these issues into consideration a full 3D model, Fig 3.1, was built. The tape springs were modelled using 4-node doubly curved general-purpose shell elements (s4); 600 elements (50×12) were used to model each spring. The tape spring shell elements were generated with logarithmic bias along the tape length so that the mesh is much finer in the middle of the tapes, where most of the snap-through and contact between the tapes take place.

The elements at the end of the tapes were generated in such way that the clamped area corresponds to an integer number of elements and the nodes of these elements lie exactly on the boundary of the clamp, as shown in Fig. 3.2. Note that Δ_b and Δ_L are the width and length of the clamp, respectively.

The rolamite part of the hinge, i.e. the wheels and cable, was modelled as a set of two rigid arms using rigid beam elements. The arms connect the centres of rotation, B and C, to the clamps at A and D, Fig. 3.1. The nodes under the clamps, Fig. 3.2, are kinematically fully coupled to the nodes A and D of the rigid arms, thus creating a rigid connection between the arm and the nodes under the clamp.

Nodes B and C are fixed in all directions and can only rotate around the

1-axis. In order to simulate the hinge deformation, clockwise and anti-clockwise rotations of 90 deg. are applied to nodes B and C, respectively, see Fig. 3.3.

Contact between the tapes was modelled as a surface-to-surface contact.

The Riks solution method was initially chosen, as this is the method generally recommended for snap-through analyses. However, convergence problems were encountered after the first snap-through point. Hence, the Riks method was replaced by a displacement controlled static analysis using the stabilise option available in ABAQUS. The Stabilise option adds a fictitious mass and dashpot to each node and performs a pseudo-dynamic solution when numerical instability has been detected. This method proved to give the desired convergence.

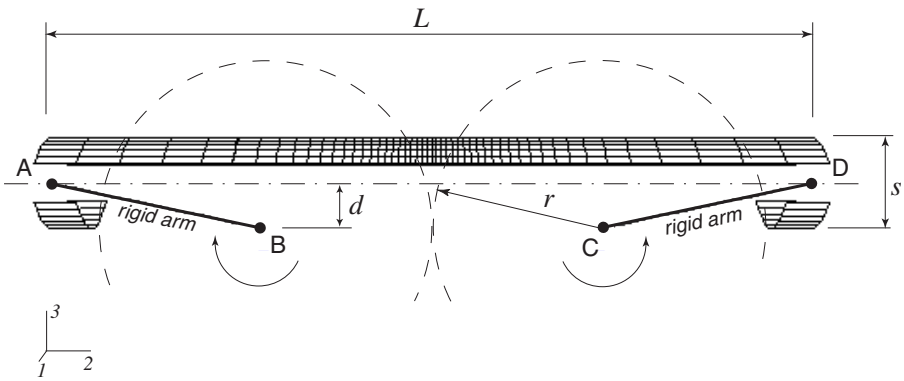

Figure 3.1: Finite element model of TSR hinge.

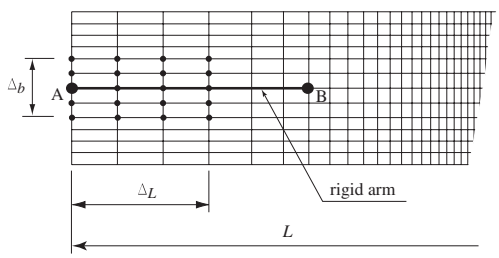

Figure 3.2: Nodes under the clamp.

3.2 Typical Finite Element Results

Figure 3.4 shows a typical moment-rotation relationship for the folding of a TSR hinge.

Due to the geometry of the hinge, at least one of the tapes is in compression. If the offset d is greater than half of the separation s, then both tapes will be in compression. As the hinge rotates, one of the tapes begins to buckle and loses a small amount of stiffness. Point B therefore represents the initial local buckling of the tape-springs. The stiffness of the hinge can also be obtained and is quite linear up to the initial point of buckling. At point C, a snap-through occurs due

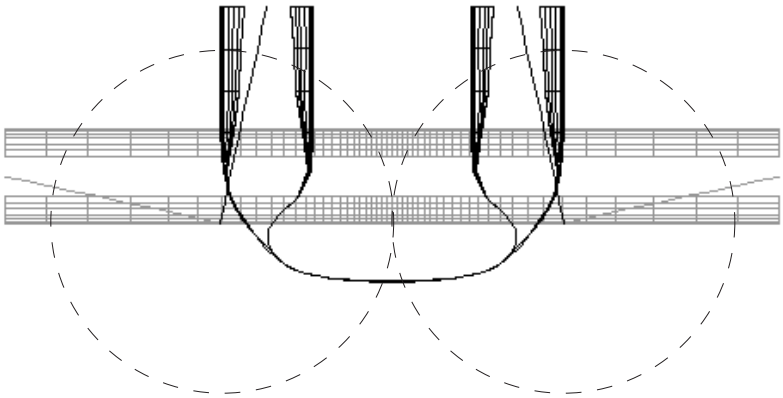

Figure 3.3: Undeformed and deformed configurations of tape springs.

to global buckling of one of the tapes. This results in a very significant loss in stiffness. As the hinge continues to fold, the stiffness continues to decrease until the moment reaches a minimum (sometimes negative) at point H. Onwards the stiffness increases fairly linearly especially once contact between the two tapes has been achieved (at point J).

Snapshots of the configurations corresponding to points A to L can be seen in Figure 3.5.

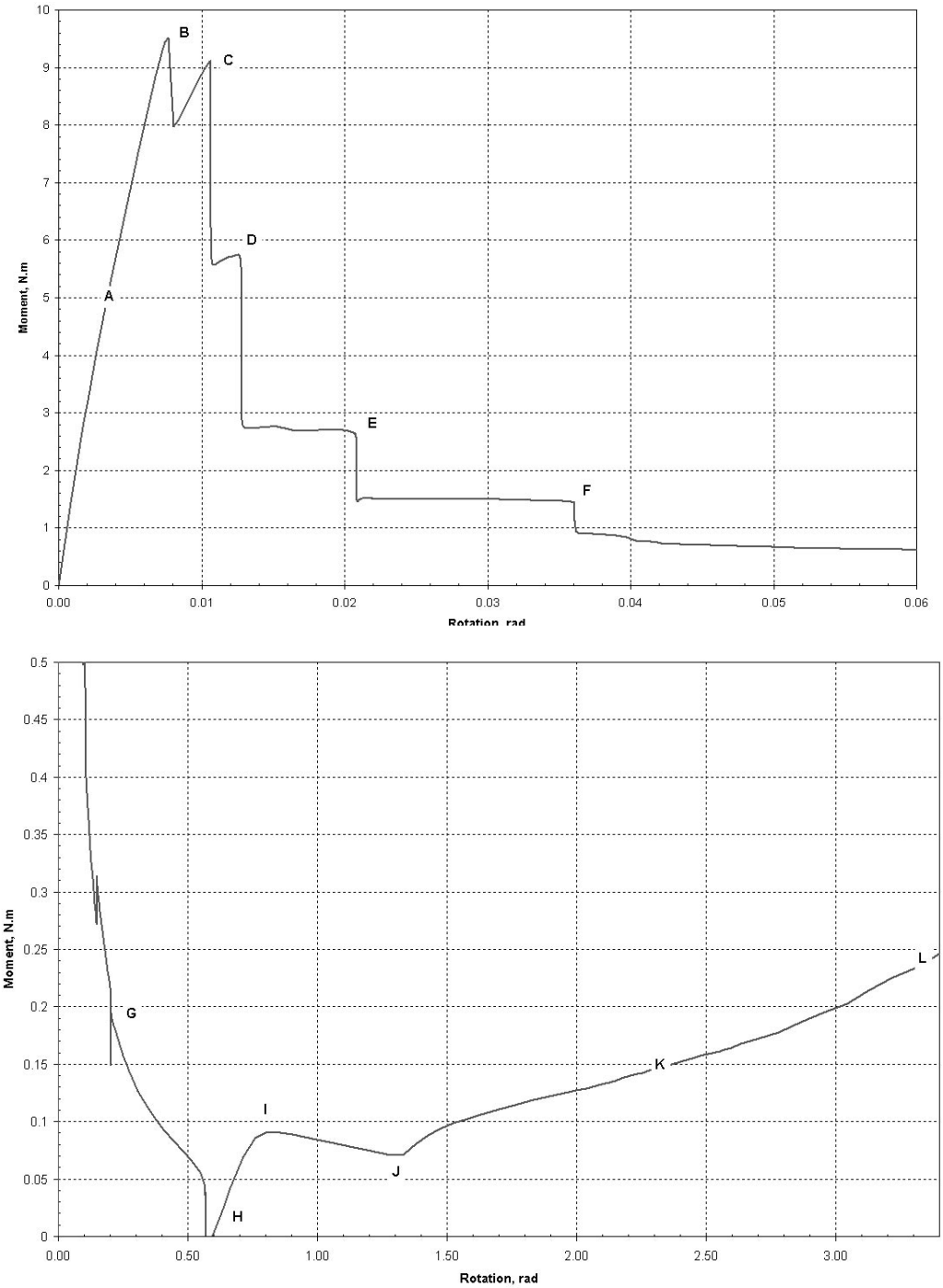

Figure 3.4: ABAQUS simulation of folding of typical TSR hinge.

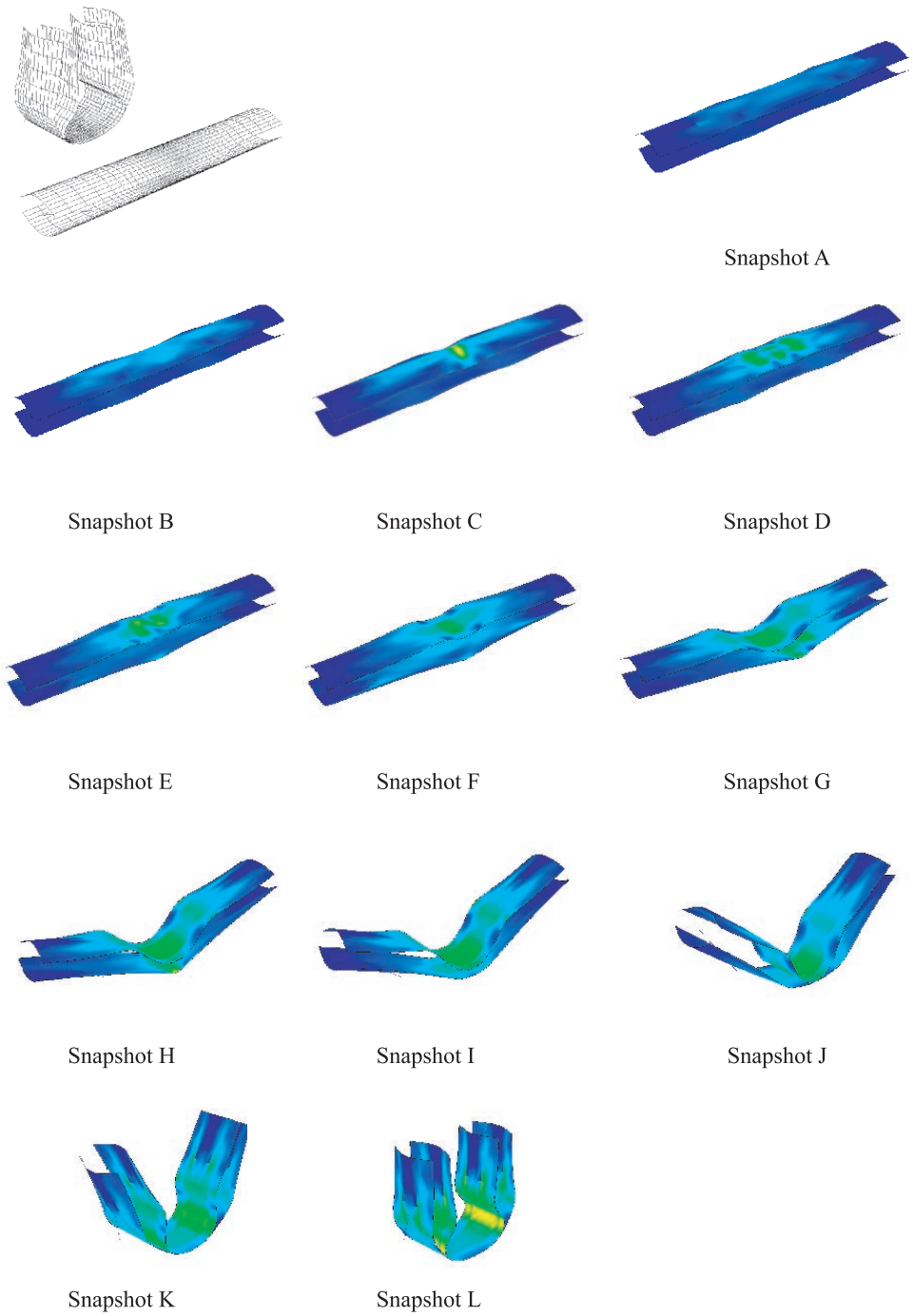

Figure 3.5: Snapshots from the simulation in Fig. 3.4.

The deployment path of the TSR hinge follows the folding path very closely until it reaches the point of snap-back to the unfolded configuration. This point

occurs at a smaller rotation than during folding.

During deployment of a TSR hinge the strain energy stored in the folded tape springs, represented by the area under the moment-rotation curve, is converted into kinetic energy. This energy increases as the hinge deploys and reaches a maximum when the rotation is zero and the hinge is in the straight configuration. At this point, if the hinge has an offset d greater than half the spacing of the tapes, then it can only snap back by folding once again.

In order to avoid snap-back, it is necessary that the energy stored in the folded configuration be less than the energy required to buckle the hinge once it has fully unfolded. The addition of external damping can help avoid this unwanted behaviour. It is interesting to note that this result is independent of the mass of any attachments to the hinge and hence of the inertial properties of the system.

Once the hinge has locked out, *i.e.* provided that it does not snap back, it will execute small amplitude oscillations in the linear range, represented by line AB in Figure 3.4. The frequency of these oscillation will depend on the mass attached to the hinge, as well as the linear stiffness of the hinge.

3.3 Experimental Set-Up

Experiments were conducted with an ESH Testing machine connected to a Schlumberger SI3531D data logger. The centre of the moment testing rig head was attached to the centre of one wheel, with the other centre of rotation of the hinge being attached to the base of the testing rig with a ball bearing. Thus, by rotating the head, a pure moment was applied to the hinge. The test set-up can be seen in Figure 3.6.

Note that in the simulation equal moments were applied to the two sides of the hinge, hence the moments predicted for one side of the hinge have to be doubled to be comparable with those measured experimentally.

Figure 3.6: Experimental apparatus to measure moment-rotation relationship.

The results from this experiment can be seen in Figures 3.10 to 3.11. It can clearly be seen in both the finite element and experimental data that the moment becomes negative at rotations of around 15°. This is undesirable, as full deployment of the hinges may be prevented if the inertia of the system

doesn't carry it through the negative-moment region. This is the reason why alternative design configurations of TSR hinges were considered, and finally version 2 was designed for the deployment tests presented in Chapter 7.

Also, although there is reasonable correlation between experiment and simulation, note that the peak "buckling" moment is over-predicted and the peak negative moment is under-predicted.

3.4 Moment-Rotation Results for Hinge Version 1

The finite element and experimental results for folding and deploying a version 1 hinge can be seen in Figures 3.7 and 3.8 respectively. The *total* rotation has been plotted, i.e. the sum of the angles rotated through by each side of the hinge.

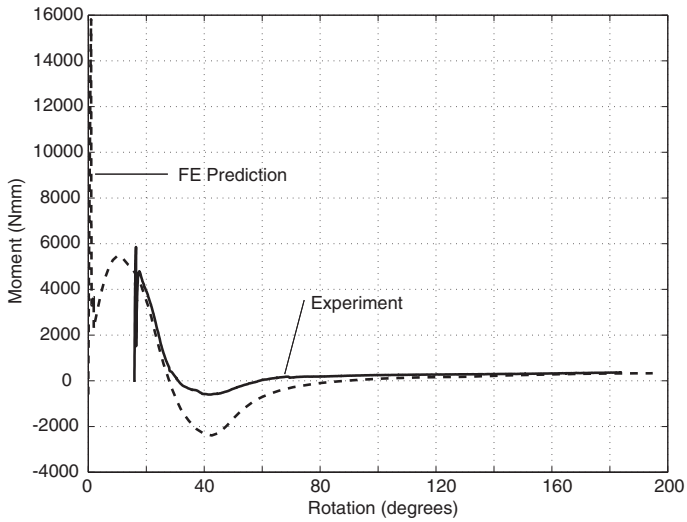

Figure 3.7: Folding of TSR hinge version 1, comparison of ABAQUS simulation and experimental results.

The FE analysis was tricky to complete as the inner tape would consistently buckle into the shape shown in Figure 3.9, which does not happen in reality. This problem was overcome by applying a small force to push the inner tape into the correct configuration; this force was removed once the correct buckled shape had formed.

The correlation between experiment and FE simulation is good for large rotations of the hinge, but for smaller rotations there are significant discrepancies. In the experiment it was not possible to reach the zero degrees configuration as there had been slippage in the experimental set-up. Hence, comparing the buckling moments from the experiment and FE analysis is of limited usefulness. The negative moments measured experimentally were not as large as those found from the simulation.

A more important point to notice about the version 1 hinge is that its moment-rotation relationship is characterised by large negative moments at low

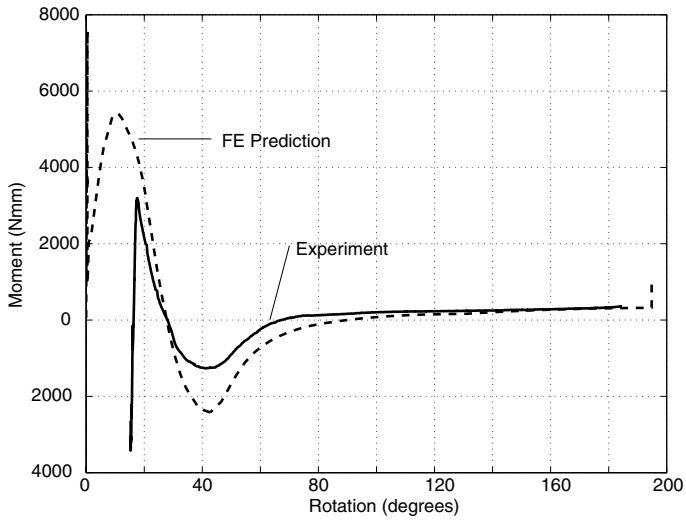

Figure 3.8: Deployment of TSR hinge version 1, comparison of ABAQUS simulation and experimental results.

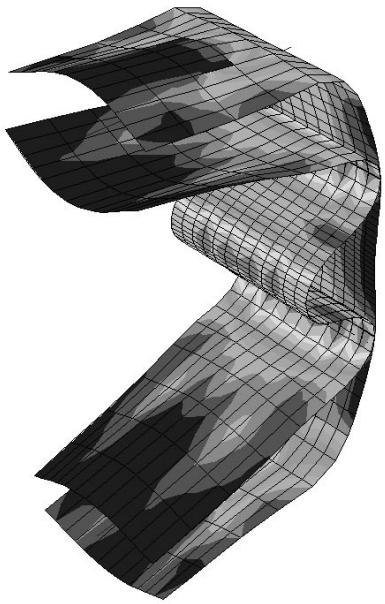

Figure 3.9: Buckling configuration of version 1 hinge if no forces are added during simulation.

angles of rotation, see Figures 3.7 and 3.8. This means that this hinge cannot be guaranteed to always deploy successfully to the straight configuration, but could become stuck at an equilibrium position in a non-zero rotation configuration. For this reason a new version of the hinge was developed, version 2, and no more effort was expended on improving the match between FE simulation and experimental results for the version 1 hinge.

3.5 Moment-Rotation Results for Hinge Version 2

The problems noted in the previous section for hinge version 1 were largely eliminated in version 2. Figures 3.10 and 3.11 show comparisons between finite element simulation and experimental measurements, respectively, during folding and deployment of the hinge. Note that the simulation, whose predictions are identical for folding and unfolding apart from the very small rotation range, predicts a small negative moment for rotations of about 35° but these were never observed in practice. Also note that the plots do not cover the full range of moments, in order to show the large-rotation response in sufficient detail.

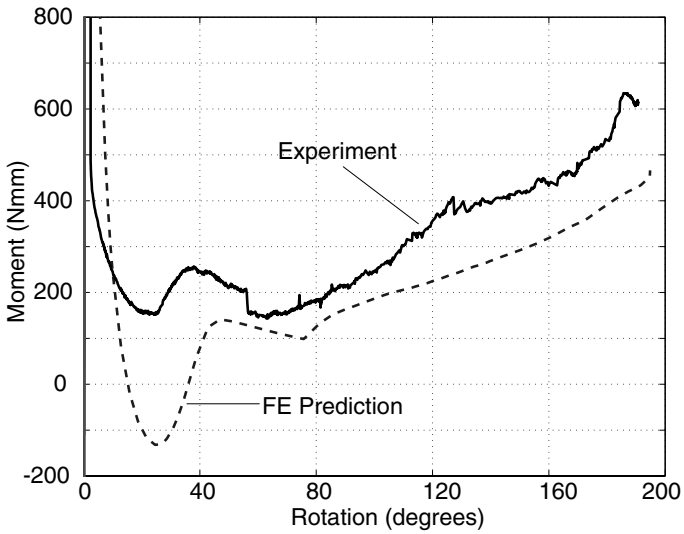

Figure 3.10: Folding of TSR hinge version 2, comparison of ABAQUS simulation and experimental results. Note that the scale on the y-axis does not show the peak moment.

The buckling moments are compared in Table 3.1. Unlike the version 1 hinge in Section 3.4, here there is quite a good correlation between the peak moments during folding; the FE simulation over-predicts by 50% which is remarkably accurate considering that we are dealing with the buckling load of a very complex structure. The peak moment during deployment is only about 10% than predicted, possibly because the elastic compliance of the Rolamite wheels and steel wires —not included in the ABAQUS model— have a significant effect at this stage.

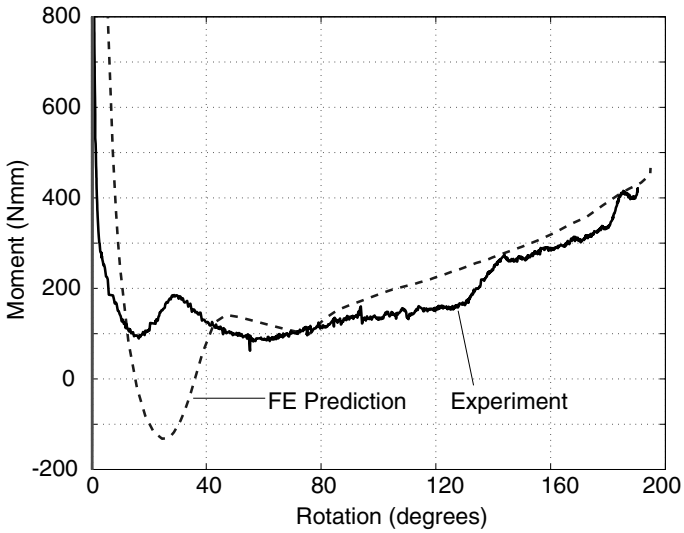

Figure 3.11: Deployment of TSR hinge version 2, comparison of ABAQUS simulation and experimental results.

Direction	Experimental	FE Analysis
Folding	13	19
Deploying	1	12

Table 3.1: Buckling moments for version 2 hinge (Nm).

Chapter 4

Parametric Study

The main objective of the parametric study was to better understand the folding behaviour of TSR hinges with different offsets d and spacing s. In this way, optimum values of these two parameters can be chosen for the design of future hinges.

The distance d was varied from 6.5 mm to 11 mm and spacings s of 14.6 mm, 15.6 mm and 16.6 mm were considered. Moreover, a simplified moment-rotation relationship was defined, which is defined by only 5 pairs of moment/rotation values.

4.1 Simplified Model

A simplified model defined by five points and five straight lines can be used to approximate the folding of a TSR hinge. This model is shown in Figure 4.1.

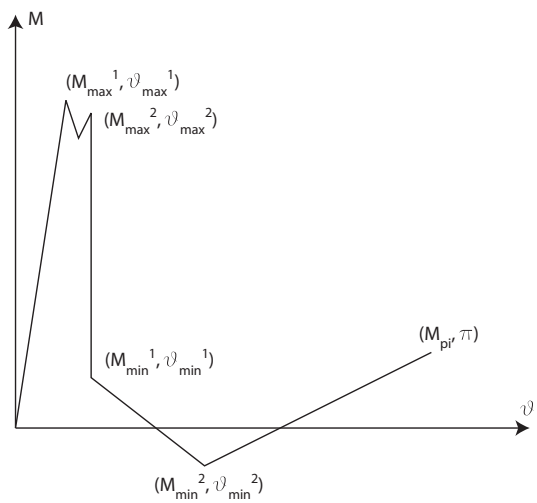

Figure 4.1: Simplified model for the folding of a TSR hinge.

4.2 Results

A series of 18 fully non-linear analyses was carried out in ABAQUS, in order to derive the moment-rotation pairs required to set up the simple model. Six values of offset were considered: $d = 6.5,\ 7,\ 8,\ 9,\ 10$ and 11 mm. For each offset, three values of spacing were also considered: $s = 14.6, 15.6$ and 16.6 mm. Note that for a spacing of 15.6 mm, $d > 8$ mm will ensure that both tapes are in compression during folding.

A large set of results is shown in Figure 4.2. They show that varying the spacing s has only a fairly small effect on the folding of the hinge. The only significant difference is in the values of M^2_{min}. The plots show that, if an offset $d = 8$ mm is chosen, any of the spacings would be satisfactory.

More interesting results have been plotted in Figures 4.3 and 4.4. These figures show clearly that increasing the distance also increases the initial stiffness of the hinge but decreases the stiffness for rotations greater 0.5 rad.

Moreover, the greater the distance, the lower the minimum moment, even becoming negative for $d > 9$ mm. This is an undesirable feature, as it is possible that the hinge could lock prematurely since an intermediate equilibrium position would exist along the folding or unfolding path.

Another interesting feature is that the stiffness between points M^2_{min} and M_{pi} is the same and the curves are therefore only shifted up or down relative to each other.

By inspection of these curves, $d = 8$ mm appears to be the most suitable offset since the moment remains fairly constant around the point M^2_{min} and does not become negative. Unfortunately, this result was not yet available when the version 1 hinge was being re-designed, hence it was not incorporated in the version 2 hinge.

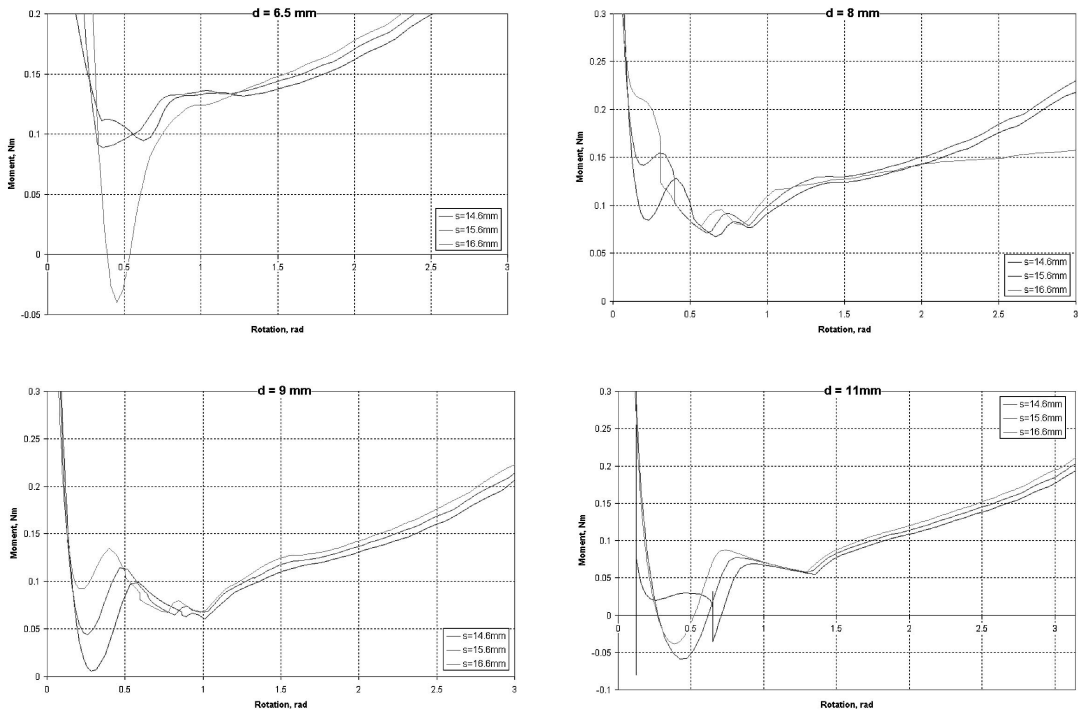

Figure 4.2: Effect of d and s on folding behaviour.

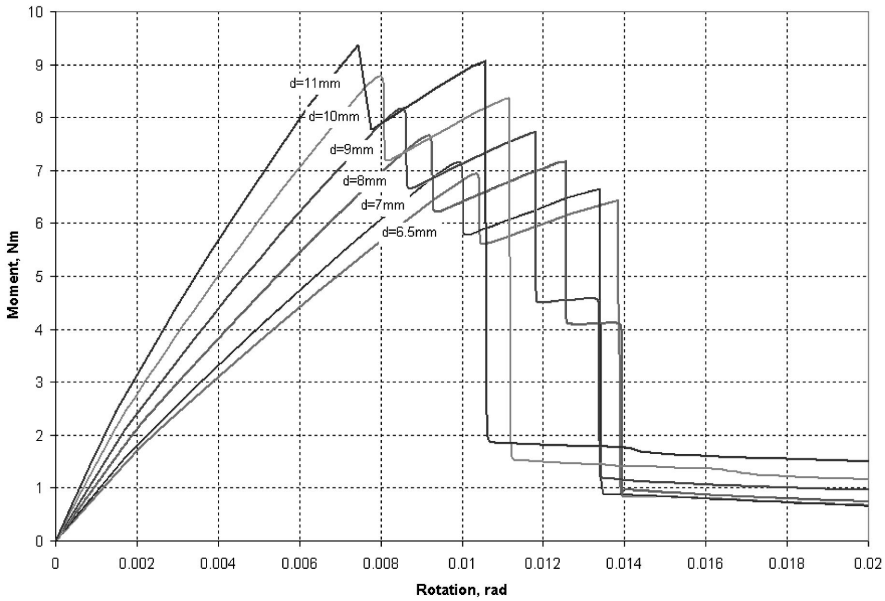

Figure 4.3: Effect of varying d, small rotation range, for s=15.6 mm.

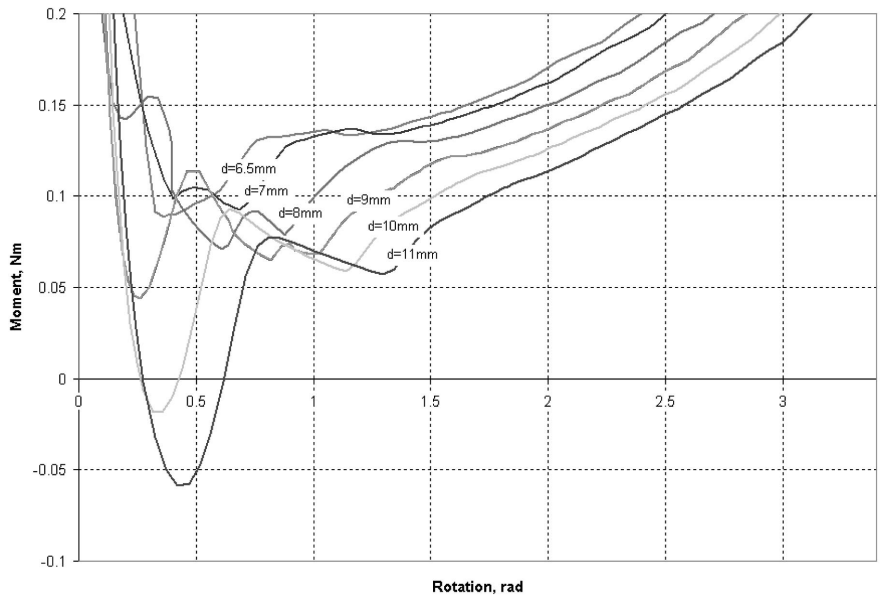

Figure 4.4: Effect of varying d, large rotation range, for s=15.6 mm.

4.3 Equation for M^1_{max}

By carefully recording all the values for all the key points in the simplified model, it is possible to assess their variation and propose some preliminary equations that could be used to interpolate between the values that have been calculated. With further work, it is likely that these equations could be put in a more compact form.

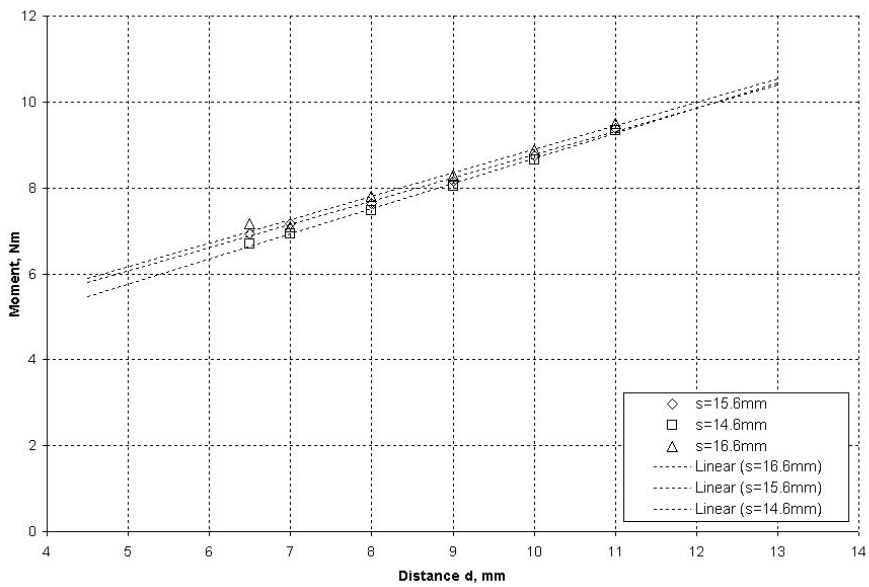

Figure 4.5: Variation of M^1_{max} with offset.

It is evident from Figure 4.5 that there is a simple relationship between M^1_{max} and offset d. It is therefore possible to propose the following linear regression equations

$$s = 14.6\ mm, \qquad M^1_{max} = 0.5845d + 2.8426 \tag{4.1}$$

$$s = 15.6\ mm, \qquad M^1_{max} = 0.54d + 3.37 \tag{4.2}$$

$$s = 16.6\ mm, \qquad M^1_{max} = 0.5454d + 3.4406 \tag{4.3}$$

4.4 Equation for ϑ^1_{max}

In this case, the rotations vary approximately in a logarithmic manner.

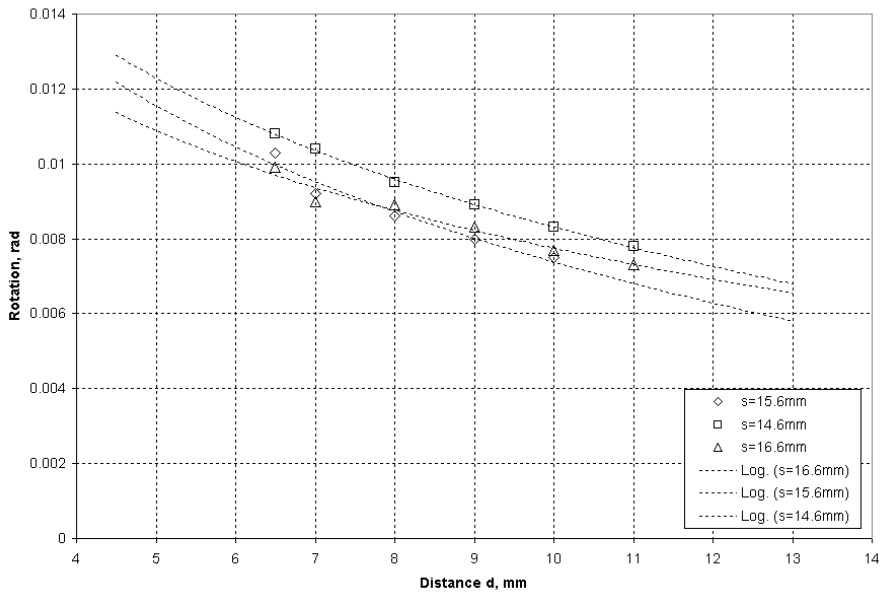

Figure 4.6: Variation of ϑ^1_{max} with offset d.

$$s = 14.6\ mm, \qquad \vartheta^1_{max} = -0.0057 \ln d + 0.0215 \tag{4.4}$$

$$s = 15.6\ mm, \qquad \vartheta^1_{max} = -0.006 \ln d + 0.0212 \tag{4.5}$$

$$s = 16.6\ mm, \qquad \vartheta^1_{max} = -0.0045 \ln d + 0.0182 \tag{4.6}$$

4.4.1 Equation for M_{max}^2

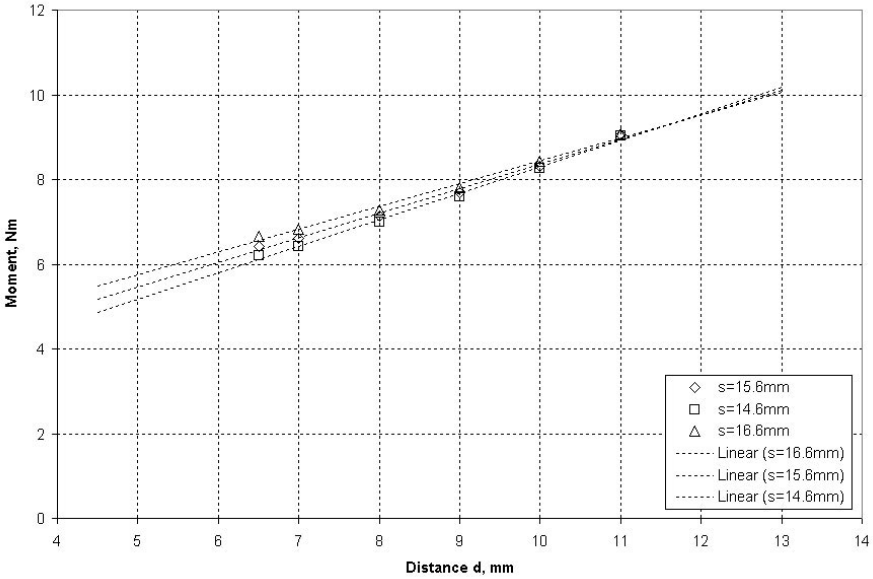

Figure 4.7: Variation of M_{max}^2 with offset d.

$$s = 14.6\ mm, \qquad M_{max}^2 = 0.6241d + 2.0597 \tag{4.7}$$

$$s = 15.6\ mm, \qquad M_{max}^2 = 0.5813d + 2.5508 \tag{4.8}$$

$$s = 16.6\ mm, \qquad M_{max}^2 = 0.5392d + 3.0521 \tag{4.9}$$

4.4.2 Equation for ϑ^2_{max}

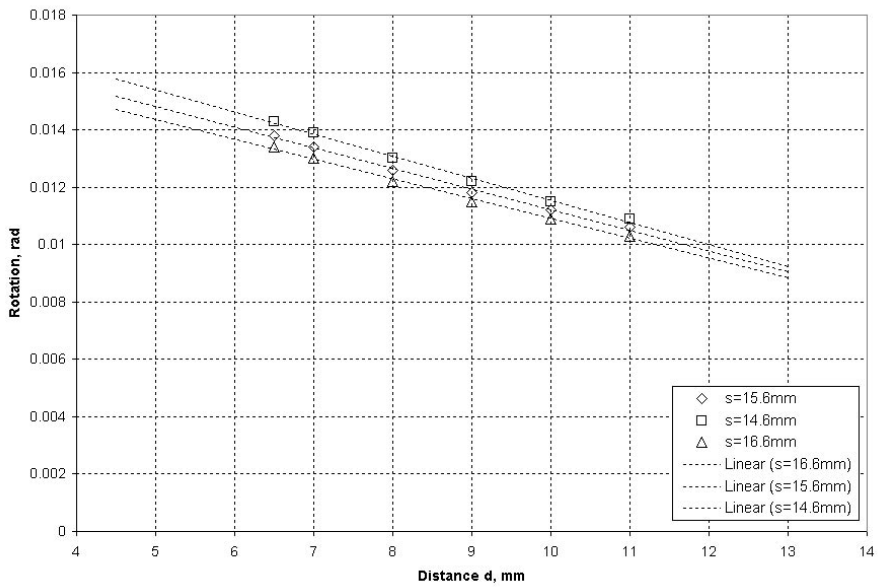

Figure 4.8: Variation of ϑ^2_{max} with offset d

$$s = 14.6\ mm, \qquad \vartheta^2_{max} = -0.0008d + 0.0192 \tag{4.10}$$

$$s = 15.6\ mm, \qquad \vartheta^2_{max} = -0.0007d + 0.0184 \tag{4.11}$$

$$s = 16.6\ mm, \qquad \vartheta^2_{max} = -0.0007d + 0.0178 \tag{4.12}$$

4.4.3 Equation for M^1_{min}

In this case, one of the points was considered an outlier and hence was excluded in the derivation of the regression equations.

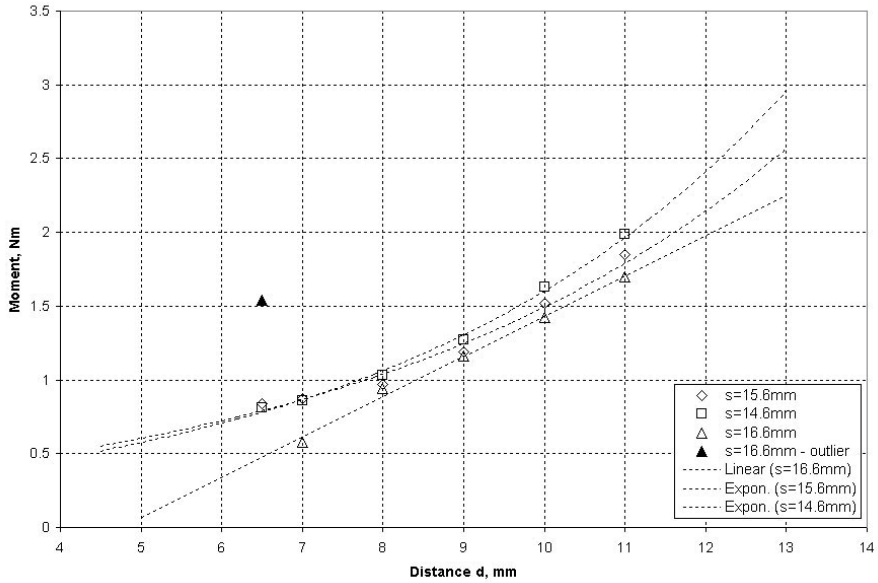

Figure 4.9: Variation of M^1_{min} with offset d.

$$s = 14.6\ mm, \qquad M^1_{min} = 0.2065e^{0.2048d} \tag{4.13}$$

$$s = 15.6\ mm, \qquad M^1_{min} = 0.2441e^{0.1811d} \tag{4.14}$$

$$s = 16.6\ mm, \qquad M^1_{min} = 0.272d - 1.288 \tag{4.15}$$

4.4.4 Equation for ϑ^1_{min}

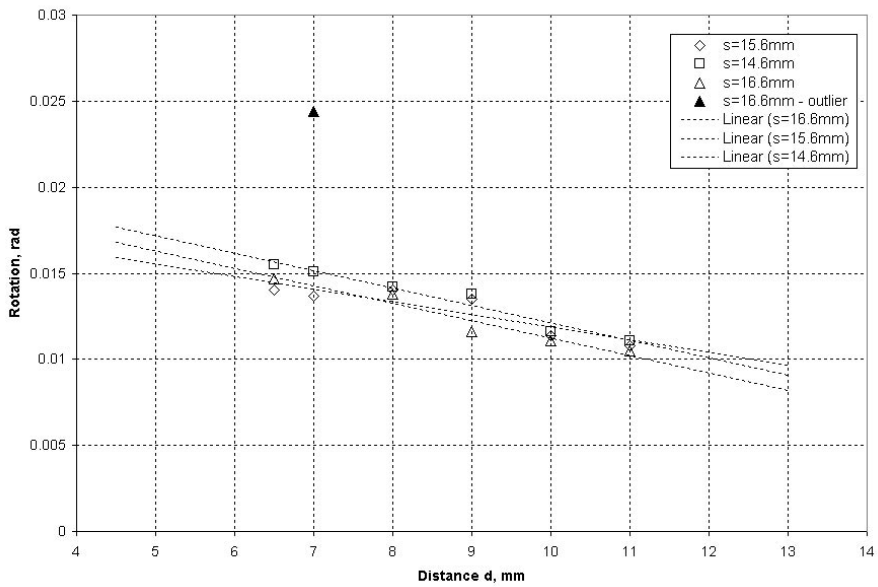

Figure 4.10: Variation of ϑ^1_{min} with offset d.

$$s = 14.6\ mm, \qquad \vartheta^1_{min} = -0.001d + 0.0223 \tag{4.16}$$

$$s = 15.6\ mm, \qquad \vartheta^1_{min} = -0.0007d + 0.0192 \tag{4.17}$$

$$s = 16.6\ mm, \qquad \vartheta^1_{min} = -0.001d + 0.0213 \tag{4.18}$$

4.4.5 Equation for M^2_{min}

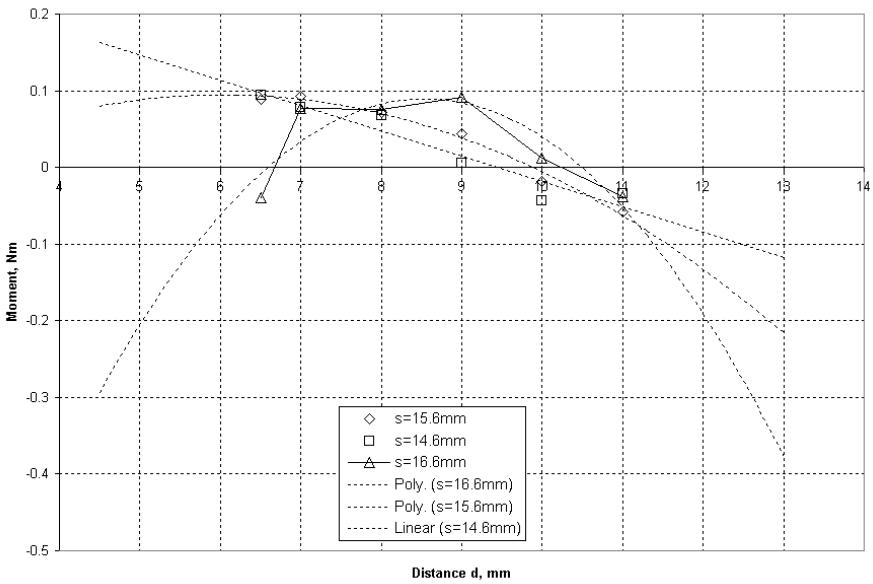

Figure 4.11: Variation of M^2_{min} with offset d.

$$s = 14.6\ mm, \qquad M^2_{min} = -0.0329d + 0.3108 \tag{4.19}$$

$$s = 15.6\ mm, \qquad M^2_{min} = -0.0064d^2 + 0.0771d - 0.1377 \tag{4.20}$$

$$s = 16.6\ mm, \qquad M^2_{min} = -0.0234d^2 + 0.4005d - 1.6213 \tag{4.21}$$

4.4.6 Equation for ϑ^2_{min}

For the case of ϑ^2_{min}, the relationship is not well defined. The equations must therefore be used with great caution until further work has been carried out. It is nevertheless possible to use these results as upper- or lower-bound estimates of ϑ^2_{min}.

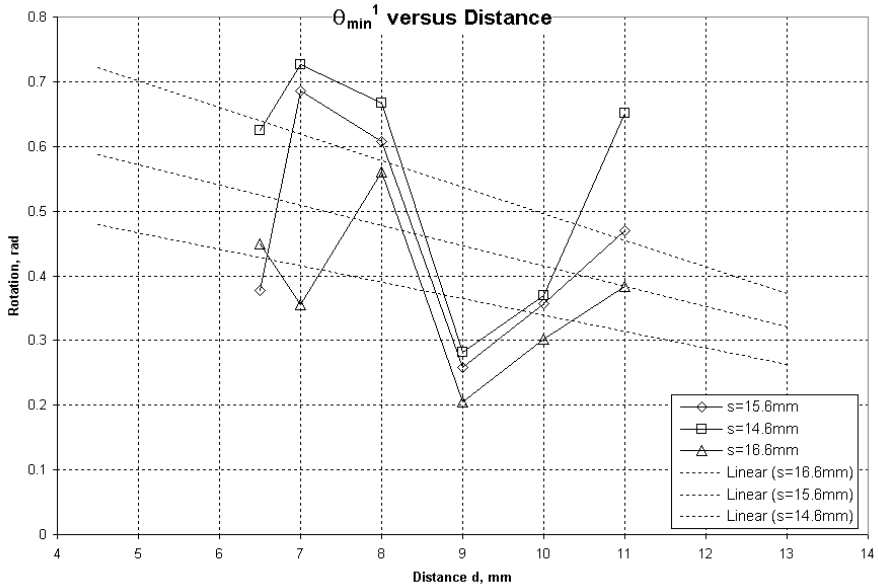

Figure 4.12: Variation of ϑ^2_{min} with offset d.

$$s = 14.6\ mm, \qquad \vartheta^2_{min} = -0.041d + 0.9055 \tag{4.22}$$

$$s = 15.6\ mm, \qquad \vartheta^2_{min} = -0.0312d + 0.7275 \tag{4.23}$$

$$s = 16.6\ mm, \qquad \vartheta^2_{min} = -0.0254d + 0.5936 \tag{4.24}$$

4.4.7 Equation for M_{pi}

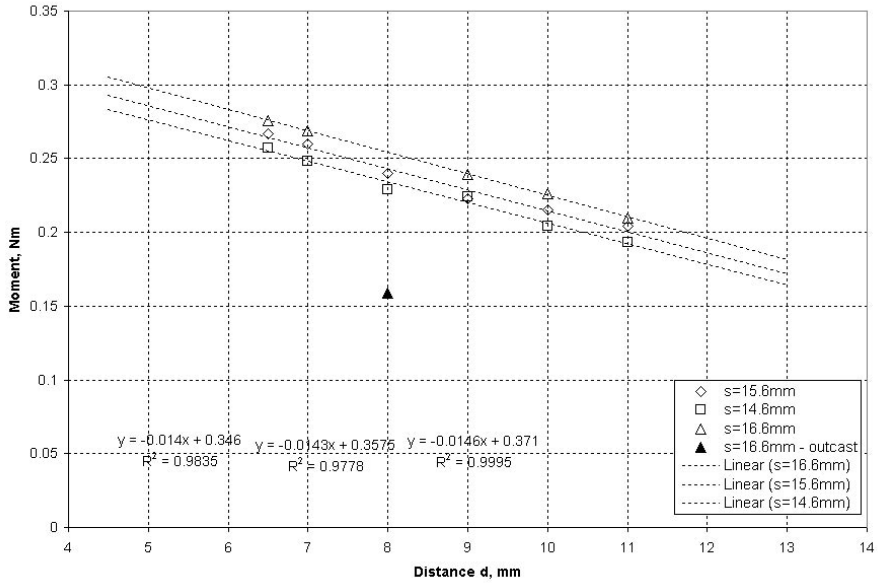

Figure 4.13: Variation of M_{pi} with offset d.

$$s = 14.6\ mm, \qquad M_{pi} = -0.014d + 0.346 \tag{4.25}$$

$$s = 15.6\ mm, \qquad M_{pi} = -0.0143d + 0.3575 \tag{4.26}$$

$$s = 16.6\ mm, \qquad M_{pi} = -0.0146d + 0.371 \tag{4.27}$$

Chapter 5

Deployed Stiffness of Hinge

Knowledge of the deployed stiffness of TSR hinges is required in order to predict the overall stiffness and hence natural frequency of any deployable appendage that is supported through such hinges.

The deployed stiffness of a TSR hinge was measured and predicted by a number of methods, including hand calculations and finite element analysis. Both the analysis and tests were made for the tapes and the Rolamite part of the hinge, on their own, as well as for the whole hinge, to obtain a better understanding of the contribution made by the separate parts. A summary of the results can be seen in Table 5.1 (the x, y and z-axes are defined in Figure 5.1). The work presented in this chapter was started long before the version 2 hinge became available, hence version 1 was used.

	Measurements			Predictions			
Direction	Tapes	Rolamite	**TSR**	Tape	Rolamite	**TSR**	Units
K_{xx}	5400	1768	**9216**	10363	1040	**11403**	N/mm
K_{yy}	236	31.9	**221**	425	40	**465**	N/mm
K_{zz}	9.66	115	**134**	23	160	**183**	N/mm
T_{xx}	29	40	**75**	31	70	**101**	Nm/rad
T_{yy}	114	0	**240**	426	0	**900**	Nm/rad
T_{zz}	480	360	**782**	451	735	**1186**	Nm/rad

Table 5.1: Summary of deployed stiffness results.

5.1 Axial Stiffness

Experimental Values

The extensional stiffness is denoted by K_{xx}. Experimental measurements were obtained by using the attachment pieces shown in Figure 5.2 to connect one side of the hinge to the cross-head of an Instron 5564 Testing machine and the other to the base of the Instron. The hinge was then tested in tension and compression, and force-extension relationships were obtained for the Rolamite body, tape-spring and complete TSR hinge, see Figures 5.3 to 5.5 respectively.

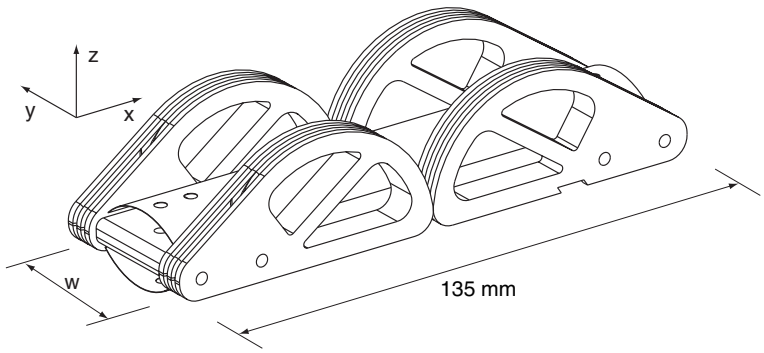

Figure 5.1: Definition of coordinate system for the hinge.

Stiffness values were defined from the gradients of these curves, as shown by a dotted line on the respective force-extension curves, and the measured stiffness of the test set-up (11348 N/mm) was accounted for.

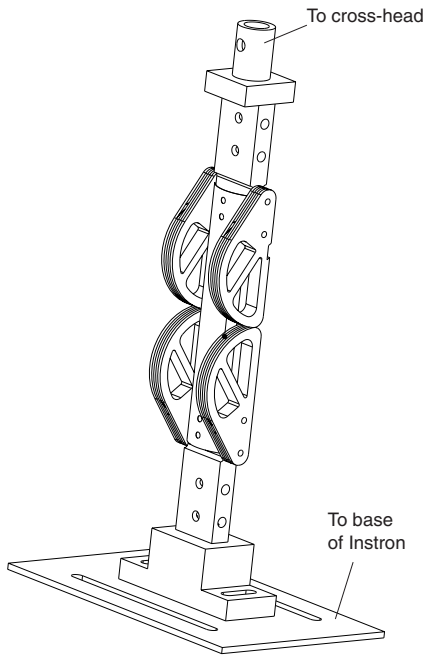

Figure 5.2: K_{xx} test set-up

Prediction of Rolamite Stiffness

The stiffness of the Rolamite part of the hinge was found by a number of methods. A finite element model of the hinge utilising contact analysis theory at the join between the two hinge elements was made in Pro/Mechanica (Parametric Technology, 2000). This model was based on the Pro/Engineer manufacturing model, consisting of 2940 "tetra" elements and can be seen in Figure 5.6. Only one half of the hinge was analysed, with the overall stiffness found by

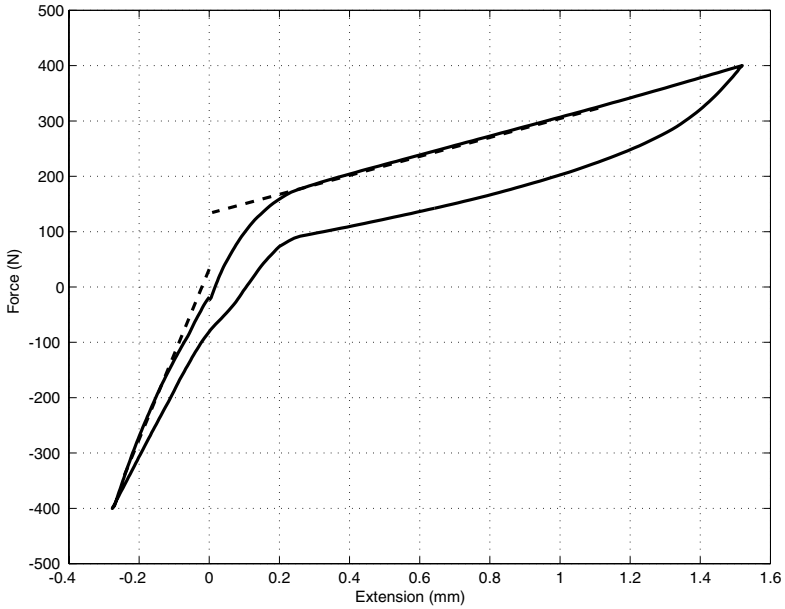

Figure 5.3: K_{xx} Rolamite stiffness.

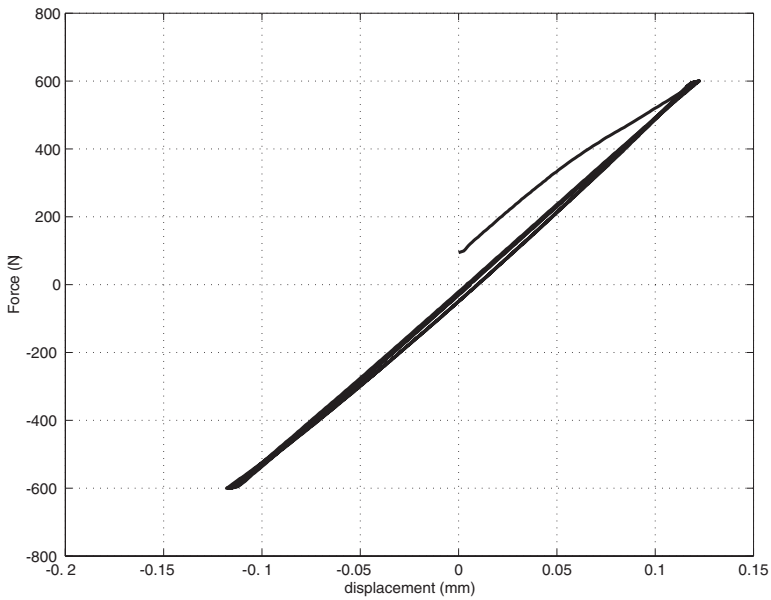

Figure 5.4: K_{xx} tape-spring stiffness.

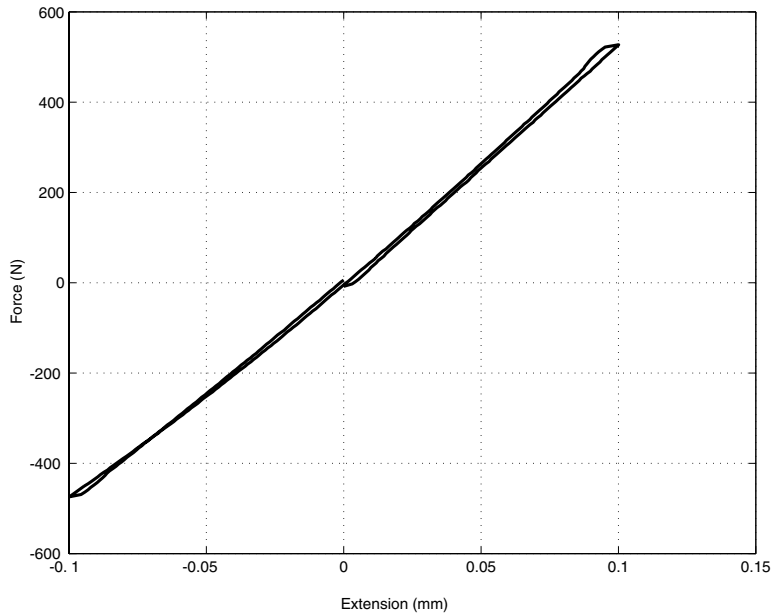

Figure 5.5: Total K_{xx} stiffness.

doubling the finite element results. This model gave a stiffness of the hinge of 1040 N/mm, which compared reasonably well with the experimental result of 1768 N/mm, although the analysis time was long due to the contact analysis and the large number of elements arising from the complex geometry of the hinge.

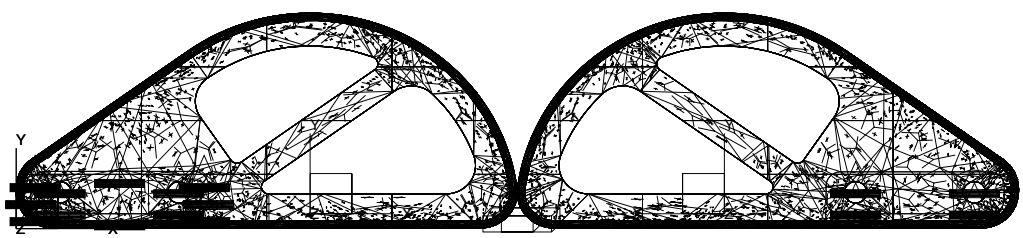

Figure 5.6: Pro/Mechanica Rolamite finite element model.

In order to allow a quicker analysis of possible future hinge designs, an analytical model of the hinge was produced. This considers each side of the Rolamite hinge as a uniform rod with dimensions as shown in Figure 5.7. K_{xxr}, the stiffness from the beam model, can then be found from

$$K_{xxr} = 2\frac{A_{eq}E}{L} \tag{5.1}$$

where A_{eq} is the cross-sectional area of one of the two rods, L the length and E the Young's Modulus of the Rolamite material.

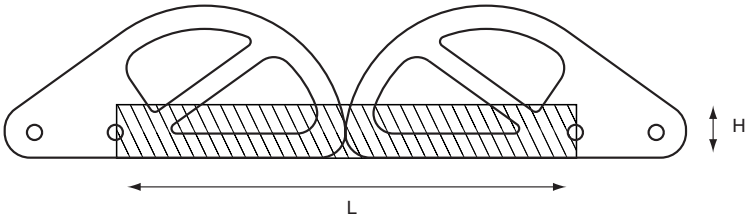

Figure 5.7: Equivalent beam (hatched) for Rolamite analysis.

For $A_{eq} = 80$ mm^2, $L = 88$ mm and $E = 3.1$ kN/mm^2 (Delrin), K_{xxr} is equal to 5636 N/mm. This was then compared to the results from a finite element analysis as described above but with the hinges rigidly connected together rather than having a deformable contact area. This model resulted in a stiffness of 5000 N/mm, showing reasonable agreement.

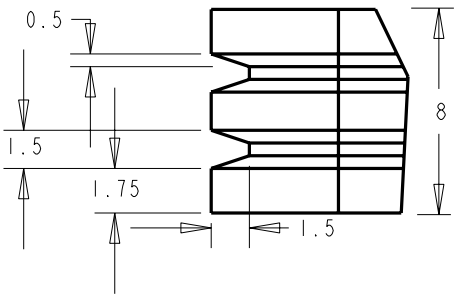

Figure 5.8: Contact area of Rolamite hinge.

It is obvious that the loss of stiffness due to the hertzian contact needs to be included into the analysis to gain an accurate prediction of the stiffness. The contact area of the hinge is shown in Figure 5.8 and it can be seen that the total width of the contact area (for two sides of the hinge) is 10 mm, made up of four 1.75 mm wide areas and two 1.5 mm areas. As the contact areas are narrow, it is best to use the contact analysis for the ends of each of the small cylinders being in a state of plane stress with the centers in plane strain. The total compression, δ, can then be found from (Johnson, 1987)

$$\delta = \left(\frac{a^2}{2R}\right)\left(2\ln\left(\frac{4R}{a}\right) - 1\right) \tag{5.2}$$

where R is the radius of curvature of the contact area and the semi-contact width, a, is found from

$$a^2 = \frac{4QR}{\pi b E^*} \tag{5.3}$$

where Q is the load, b the width of contact area and E^* is the composite Young's Modulus.

The stiffness of the Rolamite due to the contact area is then found from

$$K_{xxc} = \frac{Q}{\delta} \tag{5.4}$$

As the contact stiffness and the beam stiffness are acting as springs in series the overall stiffness of the Rolamite can be found from

$$K_{xx} = (K_{xxc}^{-1} + K_{xxr}^{-1})^{-1} \tag{5.5}$$

For $R = 28.1$ mm, $W = 10$ mm and $E = 3.1$ kN/mm^2 K_{xx}, K_{xxr} and K_{xxb} are plotted in Figure 5.9. It can be seen that within the expected load range of the stiffness is approximately equal to 1100 N/mm^2, which compares well with the finite element result.

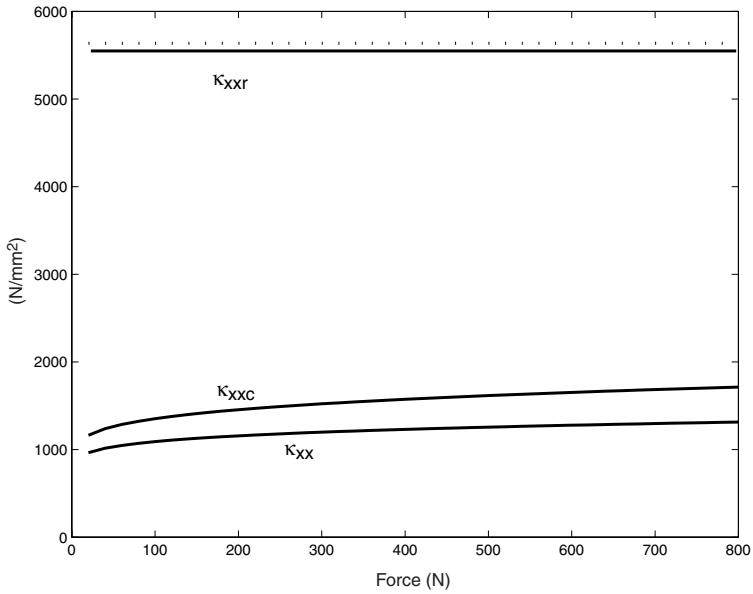

Figure 5.9: Analytical Rolamite contact analysis results.

Although the preceding analysis may only seem correct when the hinge is in compression, the pretension in the wires places the Rolamite under compression, so that the above analysis remains correct some way into the tension range. However, the analysis in incorrect at the point where the hinges have lost contact with each other and are only held together by the wires. The load at which this happens will be dependent upon the pretension in the wire.

The stiffness of the hinge when the Rolamite pieces have lost contact can be found from the relationship between the force in the wires (F_w) and the force (F_x) in the x-direction. This is found from

$$F_x = 4F_w \sin\theta \tag{5.6}$$

where θ is the angle that the wires make with the x-direction and the factor 4 is because there are 4 wires. F_w can be found, assuming that there are no appreciable geometry changes, from

$$F_w = \frac{E_w A_w \delta_x \cos\theta}{L_w} \tag{5.7}$$

where E_w is the Young's modulus of the wire, A_w the cross-sectional area of the wire and L_w the length of wire that is subjected to stress. The K_{xx} stiffness due to the wires is then found from

$$K_{xx} = \frac{F_x}{\delta_x} = \frac{4E_w A_w \sin\theta \cos\theta}{L_w} \tag{5.8}$$

Using $E_w = 13200$ N/mm^2 as found from a tension test on the wire, Figure 5.10, $A_w = 0.5$ mm and $L_w = \pi R = 87.9$ mm gives $K_{xx} = 96$ N/mm. This compares to the value of 171 N/mm found from the force extension curve shown in Figure 5.3.

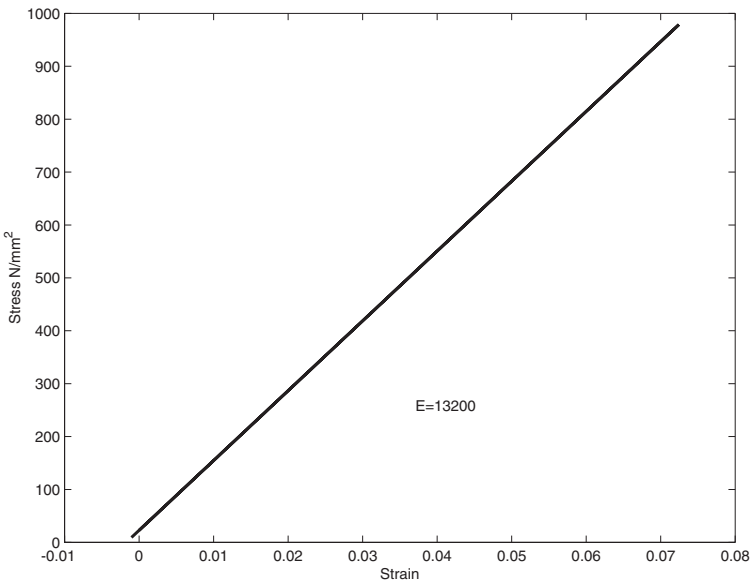

Figure 5.10: Stiffness test on coated wire used in hinge.

Prediction of Tape-Spring Stiffness

The axial stiffness of the tape-spring was predicted through a number of models. The simplest model considered the stiffness of a rod

$$K_{xx} = 2\frac{AE}{L} \tag{5.9}$$

where L is the distance between the end connections (88 mm), A the cross-sectional area of a single tape measure (2.55 mm) and E the Young's Modulus of the tape (spring steel, 210 kN/mm^2).

For these tape-measure properties, Equation 5.9 gives $K_{xx} = 12170$ N/mm, which compares to an experimental measurement of 5400 N/mm.

A finite element model of the tape-spring was made in Pro/Mechanica using the cross-sectional shape shown in Figure 5.11 and the top view shown in Figure 5.12. The model consisted of 35 3-node and 20 4-node shell elements arranged in the manner shown in Figure 5.13. This model gave $K_{xx} =$ 8596 N/mm. A similar ABAQUS model, see Figure 5.14, gave a stiffness of 10363 N/mm.

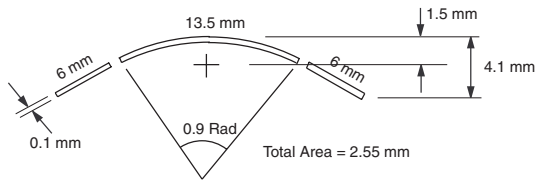

Figure 5.11: Cross-sectional shape of tape-spring used in finite element analysis.

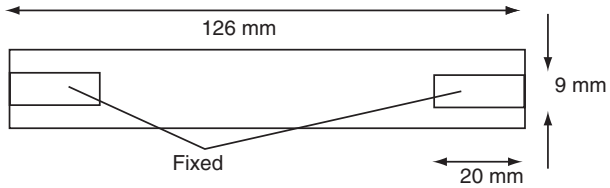

Figure 5.12: Top view of tape spring used in finite element analysis.

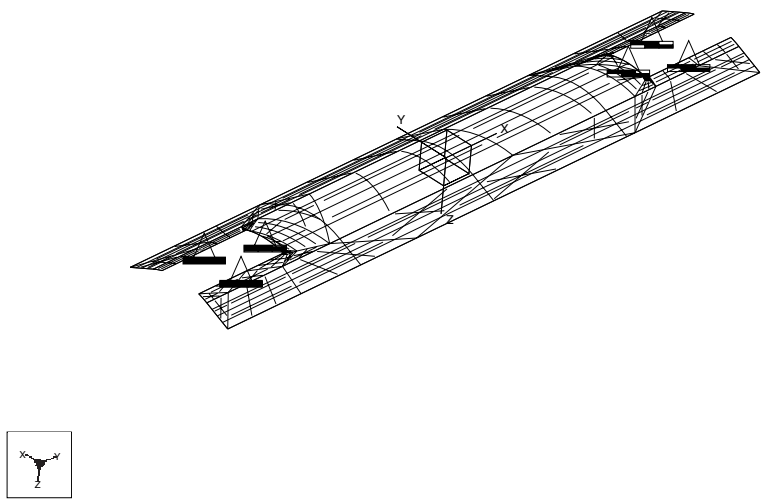

Figure 5.13: Pro/Mechanica tape-spring finite element model.

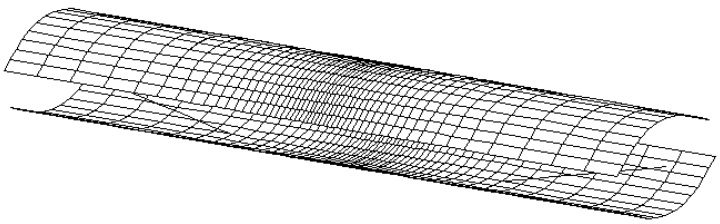

Figure 5.14: ABAQUS tape-spring finite element model.

Prediction of Total Stiffness

The total predicted stiffness was found simply by adding together the predicted Rolamite and tape-spring stiffnesses, as they act as springs "in parallel". Because of the high stiffness of the tape-springs, which has been vastly over-predicted, they dominate the final result. A total stiffness of 11403 N/mm was predicted, which differs from the practical result for the total stiffness of the hinge, 9216 N/mm, due to the poor prediction for the tape-springs.

5.2 In-Plane Shear Stiffness

Experimental Values

The in-plane shear stiffness, denoted by K_{yy}, was measured in a similar way to the axial stiffness, with the exception that the hinge was mounted at 90 degrees to the axis of the Instron. This set-up can be seen in Figure 5.15. The results of tests on the Rolamite, tape-spring and complete hinge can be seen in Figures 5.16 to 5.18 respectively. The dotted lines show the gradients from which the stiffnesses were measured.

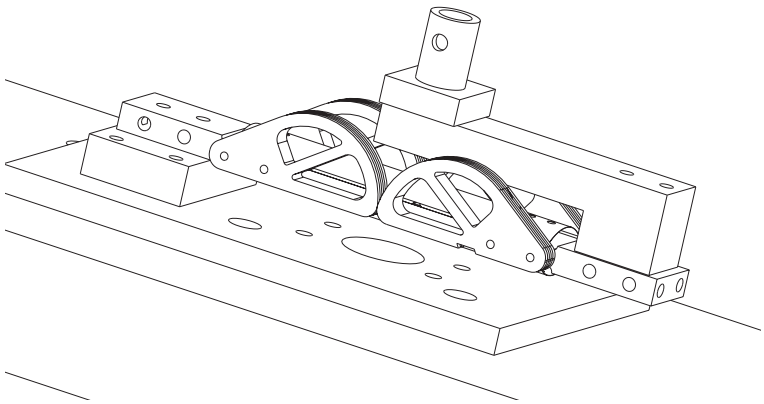

Figure 5.15: K_{yy} test set-up.

It should be noted that the increase in stiffness that can be seen in the tape-spring test, Figure 5.16, is due to contact between the Rolamite and the test set-up due to the large deflections involved; it is not a function of the Rolamite properties.

Prediction of Rolamite Stiffness

The Rolamite stiffness in the y-direction was predicted from a Pro/Mechanica model of the body of the Rolamite hinge. This model considered the two halves of the Rolamite hinge to be joined solidly together at the contact point. This analysis gave a stiffness of 40 N/mm, which compares well to the experimental value of 31.9 N/mm.

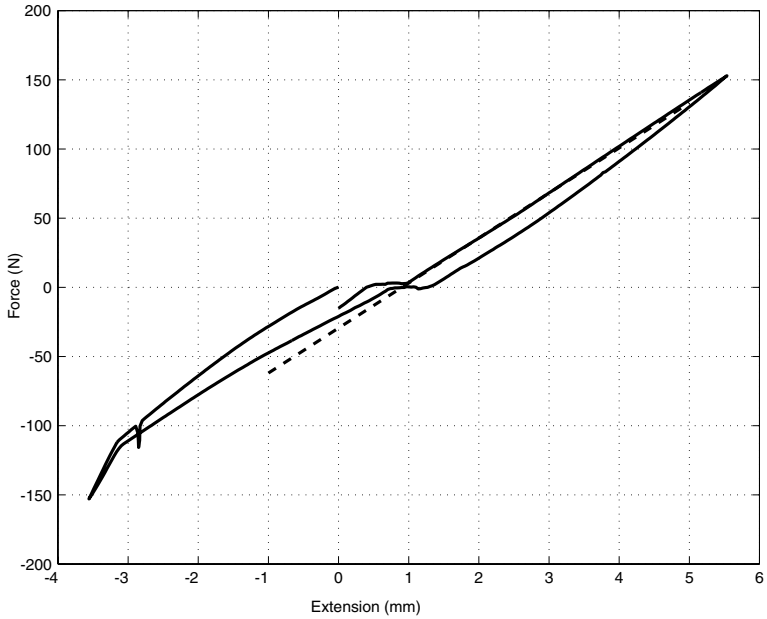

Figure 5.16: K_{yy} Rolamite stiffness.

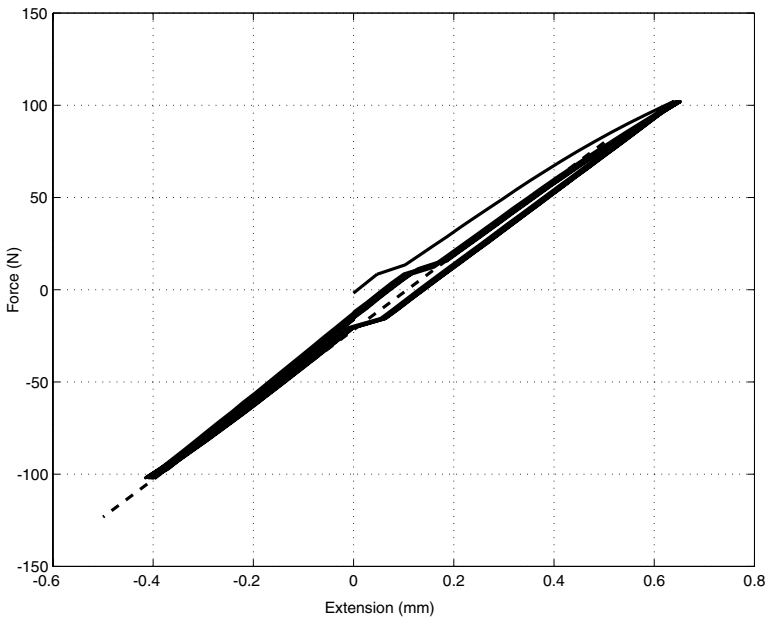

Figure 5.17: K_{yy} tape-spring stiffness.

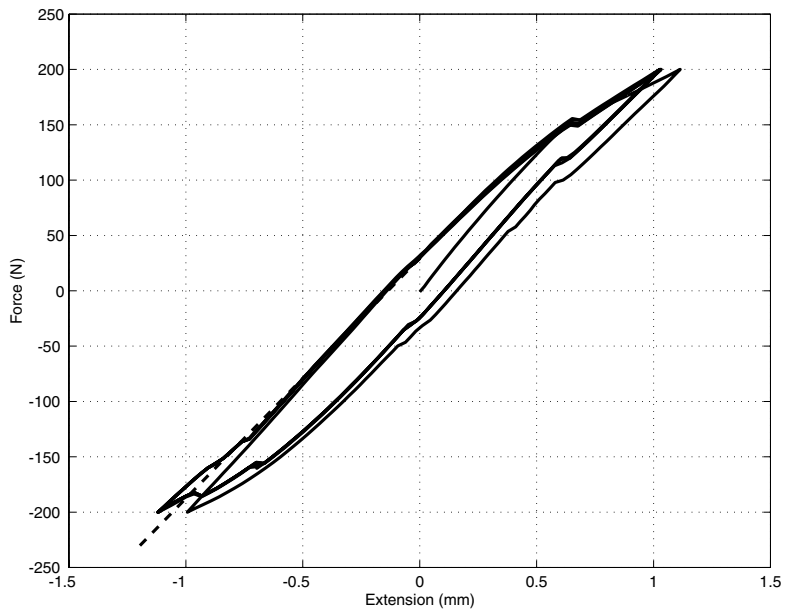

Figure 5.18: Total K_{yy} stiffness.

The stiffness K_{yy} can be found analytically by considering the two sides of the hinge separately as fixed-end beams with one of the ends undergoing a displacement, δ

$$K_{yy} = 2 \times 12EI_{zz}/L^3 \tag{5.10}$$

Using the equivalent beam developed in Section 5.1 gives an I_{zz} value of 426 mm^4. With $E = 3100$ N/mm^2 for Delrin and the equivalent beam length of 88 mm, a stiffness value of 47 N/mm was predicted.

Prediction of Tape-Spring Stiffness

The tape-spring K_{yy} stiffness was found from the same ABAQUS model already used in Section 5.1, with boundary conditions of force and displacement only in the y-direction. This model gave a stiffness of 425 N/mm, which is over twice the measured value of 200 N/mm.

K_{yy} can also be found from the formula for a fully encastre' beam

$$K_{yy} = 2\frac{12EI_{zz}}{L^3} \tag{5.11}$$

where I_{zz} is for a single tape measure; for the cross-section described in Figure 5.11 $I_{zz} = 94.56$ mm^4. Assuming a length $L = 88$ mm, measured between the ends of the connection elements, gives $K_{yy} = 699$ N/mm. By extending the length L to 108 mm, i.e. measuring the distance between the centres of the connection elements, a value of $K_{yy} = 378$ N/mm was found; this compares well with the ABAQUS prediction.

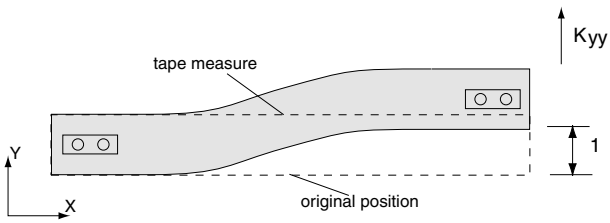

Figure 5.19: Definition of in-plane shear stiffness.

Total Stiffness

The total stiffness is found by adding together the tape-spring and Rolamite stiffnesses, which gives a predicted total stiffness of 465 N/mm. This is much higher than the practical result of 221 N/mm due to the poor prediction of the tape-spring stiffness.

5.3 Out-of-Plane Shear Stiffness

Experimental Values

The out-of-plane shear stiffness, denoted by K_{zz}, was measured in the same way as the in-plane-shear stiffness, but the hinge turned through 90 degrees; the set-up can be seen in Figure 5.20. The results of tests on the Rolamite, tape-spring and complete hinge can be seen in Figures 5.21 to 5.23. The dotted lines show the gradients from which the stiffnesses were calculated.

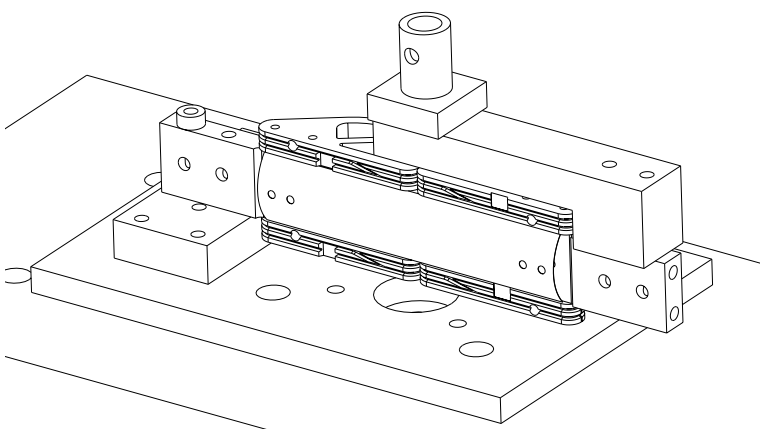

Figure 5.20: K_{zz} test set-up.

Prediction of Rolamite Stiffness

The stiffness of the Rolamite hinge was predicted by the finite element model described in Section 5.1 with the boundary conditions changed appropriately. This model predicted $K_{zz} = 160$ N/mm, which compares reasonably well to the measured stiffness of 115 N/mm.

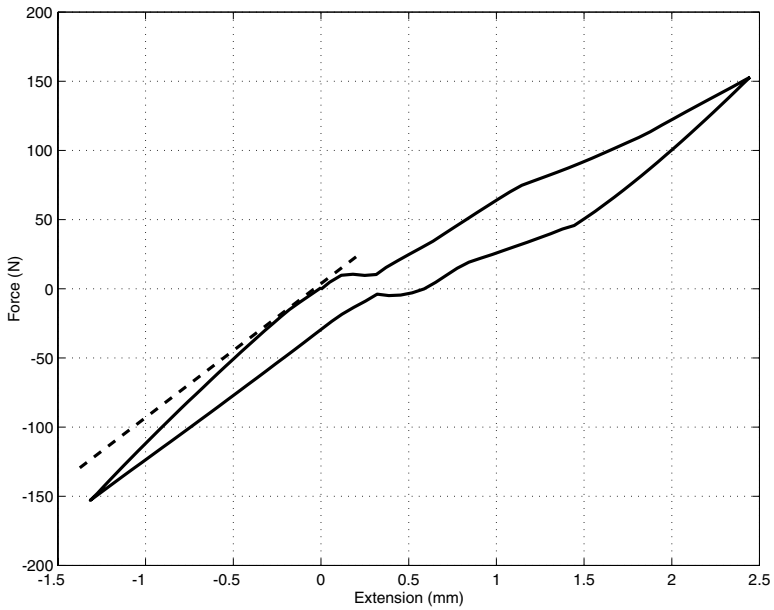

Figure 5.21: K_{zz} Rolamite stiffness.

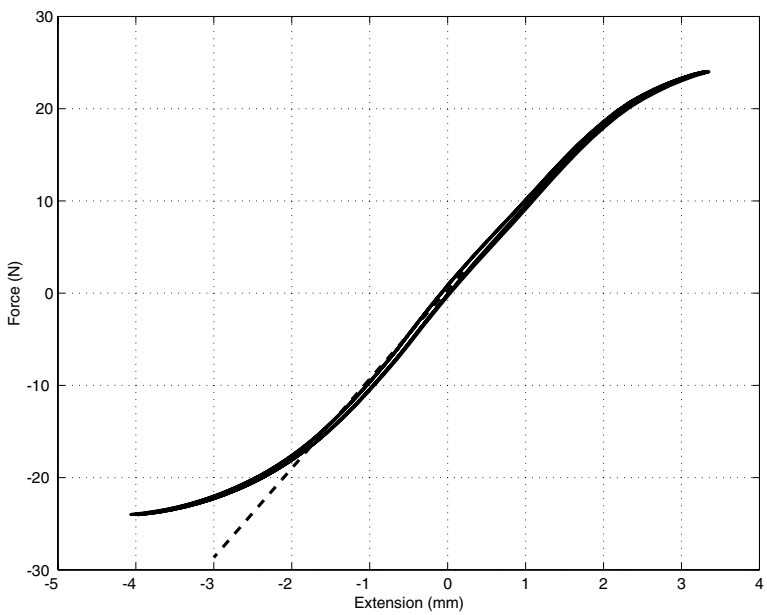

Figure 5.22: K_{zz} tape-spring stiffness.

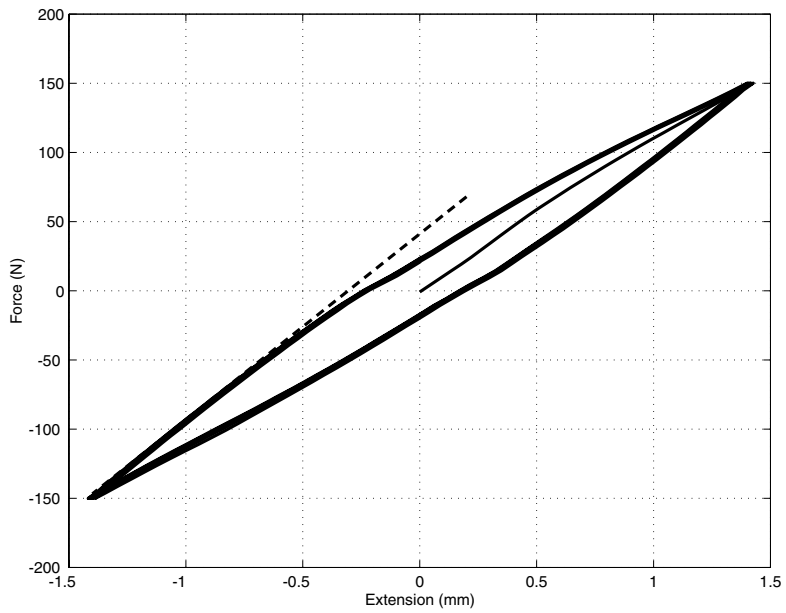

Figure 5.23: Total K_{zz} stiffness.

The analytical equivalent rod model from Section 5.1 predicts a stiffness of 72 N/mm.

The contribution to the stiffness of the hinge from the wires is approximately equal to the extensional stiffness of the wires multiplied by the number of wires and $\cos(\theta_\circ)$. This is because for a small extension of the hinge in the z-direction, it can be shown that the wires will extend by the same amount multiplied by $\cos(\theta_\circ)$ and that the stiffness is proportional to the number of wires. For this hinge the value is:

$$K_{zz} = 4A_W E_W \sin^2(\theta)/L \tag{5.12}$$

For the wire properties found in Section 5.1 the K_{zz} stiffness due to the wires was found to be 265 N/mm.

As the Rolamite body and the wires act as springs in series, the stiffness of the Rolamite is the inverse of the sum of the inverse of the stiffnesses. Using the wire stiffness and the finite element result gives a total stiffness of 99 N/mm.

Prediction of Tape-Spring Stiffness

K_{zz} was found from the ABAQUS model developed in Section 5.1, with displacement boundary conditions in the z-direction only, at the connection. This model predicted a stiffness of 22.58 N/mm, which is over twice the measured stiffness of 9.58 N/mm.

A simple analytical prediction can be obtained considering a fully encastre' beam. The K_{zz} stiffness of the tape-spring hinge is then found from

$$K_{zz} = 2\frac{12EI_{yy}}{L^3} \tag{5.13}$$

where I_{yy} is for a single tape measure. Since $I_{yy} = 4.54$ mm^4 for the cross-section described in Figure 5.11 and assuming $L = 88$ mm as before, $K_{zz} = 33.59$ N/mm was found. Again by extending L to 108 mm K_{zz} decreases to 18.16 N/mm, which compares reasonably well to the ABAQUS prediction.

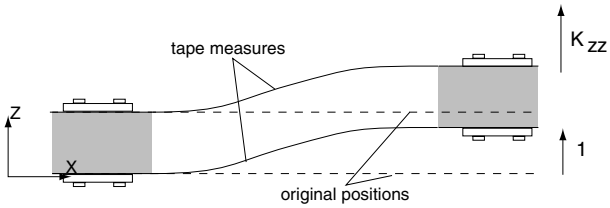

Figure 5.24: Definition of extensional stiffness in z-direction.

Total Stiffness

The total stiffness of the TSR hinge was predicted by adding the contributions of the Rolamite and tape-spring. This resulted in a predicted stiffness of 183 N/mm, compared to the experimental value of 134 N/mm.

5.4 Torsional Stiffness

The torsional stiffness, T_{xx}, is the rotational stiffness of the hinge about the x-axis.

Experimental Values

T_{xx} was measured with an FSH rotational testing machine with a Schlumberger S13531D data logger; the hinge set-up can be seen in Figure 5.25. The torque-rotation plots for the Rolamite, tape-spring and total hinge can be seen in Figures 5.26 to 5.28 with dotted lines showing the gradients from which the stiffnesses were obtained.

Prediction of Rolamite Stiffness

Consider applying a small angle of twist to the hinge, this rotation is equal to the displacement in the z-direction divided by the width, w, of the hinge, measured from the middle of the Rolamite. The moment required for this twist is the force in the z direction multiplied by w. The value of T_{xx} can then be found from

$$T_{xx} = \frac{K_{zz} w^2}{2} \tag{5.14}$$

Using the experimental value of 115 N/mm for K_{zz} and $w = 35$ mm, i.e. the distance between the centres of the two sides of the rolamite hinge, gives a stiffness of 70 Nm/rad. This compares to the measured stiffness of 40 Nm/rad.

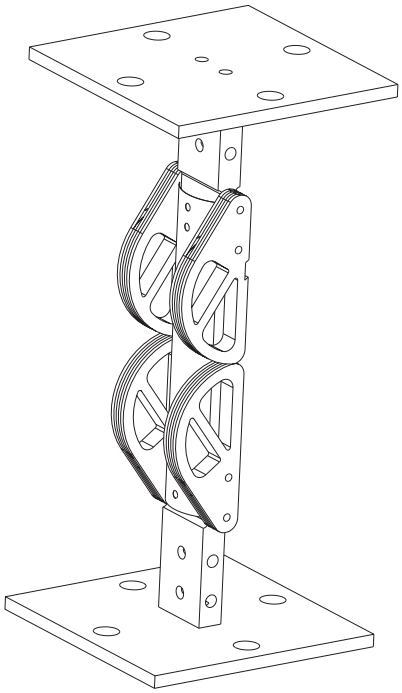

Figure 5.25: T_{xx} testing set-up

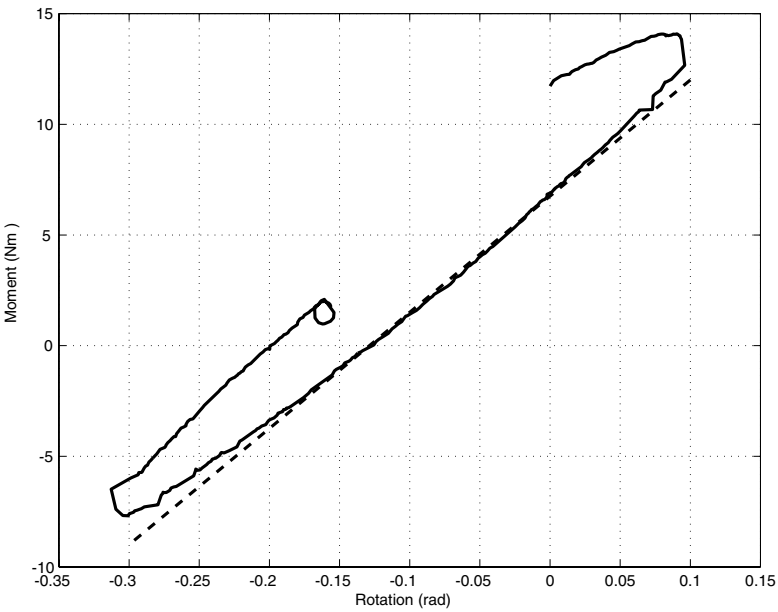

Figure 5.26: T_{xx} Rolamite stiffness.

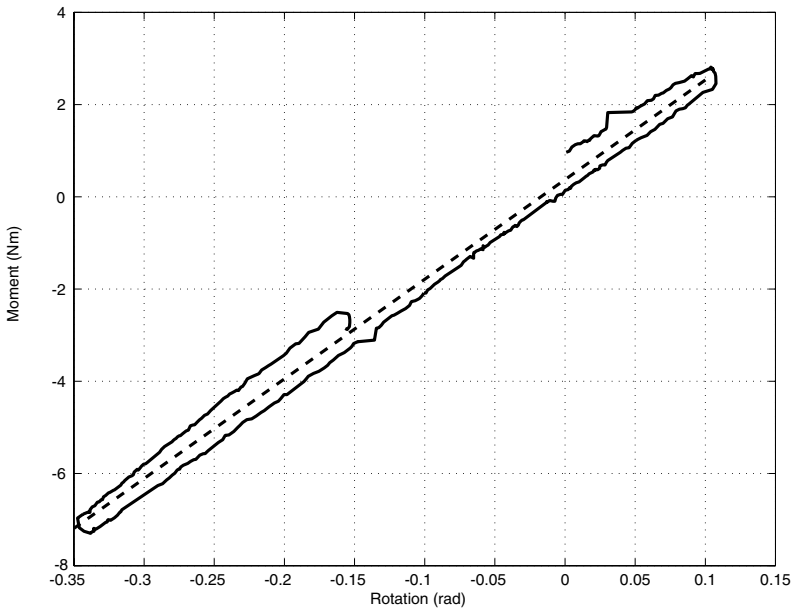

Figure 5.27: T_{xx} tape-spring stiffness.

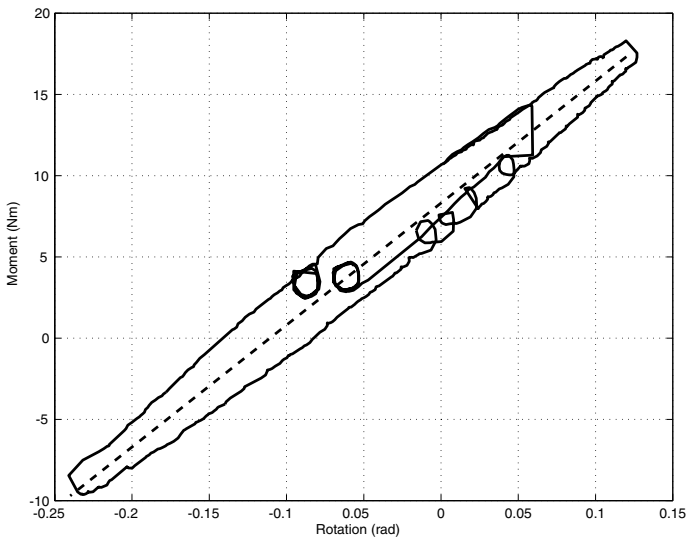

Figure 5.28: Total T_{xx} stiffness.

Prediction of Tape-Spring Stiffness

T_{xx} for the tape-springs was predicted using the ABAQUS model produced in Section 5.1, with appropriate boundary conditions. This model predicted a stiffness of 31 Nm/rad. This compares well to the stiffness of 29 Nm/rad found experimentally.

An analytical solution was found by imposing a unit rotation at the end of the hinge, corresponding to in-plane displacements of the tape-springs of $h/2$. The T_{xx} stiffness for the springs is then found from

$$T_{xx} = \frac{K_{yy}h^2}{2} \tag{5.15}$$

using a value of h, i.e. the distance between the centroids of the blades, of 12.5 mm and the K_{yy} prediction of 425 N/mm found in Section 5.2 gives a stiffness of 33 Nm/rad.

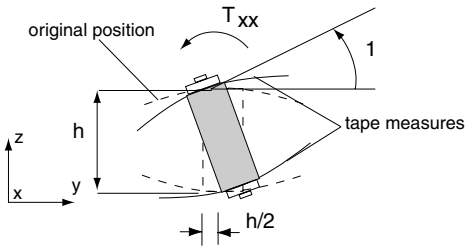

Figure 5.29: Definition of torsional stiffness.

Total Predicted Stiffness

The total hinge stiffness was predicted by adding the contributions of the Rolamite and tape-spring. This results in a predicted stiffness of 101 Nm/rad compared to the practical result of 75 Nm/rad.

5.5 In-Plane Bending Stiffness

The in-plane bending stiffness, T_{yy}, is the stiffness of the hinge bending around the y-axis.

Experimental Values

The tape-springs and the complete hinge were tested in a four-point bending test, as shown in Figure 5.30. The results can be seen below in Figures 5.31 and 5.32, respectively. The moment-rotation relationship, M, θ, was obtained from the measured force displacement displacement, F, δ, from

$$M = \frac{Fx}{2} \tag{5.16}$$

$$\theta = \frac{2\delta}{x} \tag{5.17}$$

The distance x is defined in Figure 5.30.

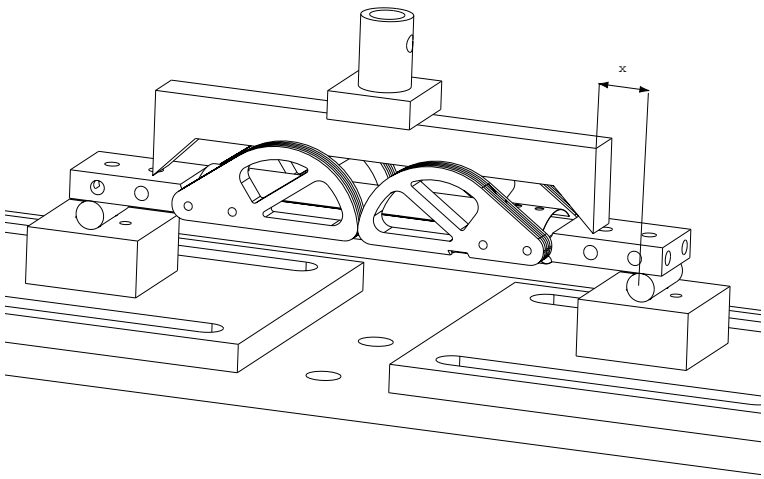

Figure 5.30: T_{yy} test set-up.

Prediction of Rolamite Stiffness

The stiffness T_{yy} of the Rolamite is zero as this is the direction of rotation of the Rolamite. However it should be noted that the Rolamite affects the stiffness of the tape-spring as it changes the boundary conditions.

Prediction of Tape-Spring Stiffness

The tape-spring stiffness T_{yy} can be predicted using the ABAQUS model developed in Section 5.1 with boundary conditions that allow free rotation about the y-axis and free translation in the z-direction. This model predicts a stiffness of 426 Nm/rad, which compares to a measurement of 114 Nm/rad.

The stiffness was also predicted by an analytical model found by assuming that one blade is compressed by $h/2$ and the other extended by $h/2$, having assumed a unit relative rotation. T_{yy} is then given by

$$T_{yy} = \frac{AEh^2}{2L} \tag{5.18}$$

For the tape-spring properties given in Section 5.1 this equation predicts a stiffness of 475 Nm/rad.

Total Predicted Stiffness

The stiffness T_{yy} of the complete hinge was predicted by assuming that the Rolamite part of the hinge is infinitely stiff and therefore constrains the hinge to rotate around the two centres of curvature of the rolling surfaces. This was modelled with ABAQUS and gave a stiffness for the hinge of 900 Nm/rad.

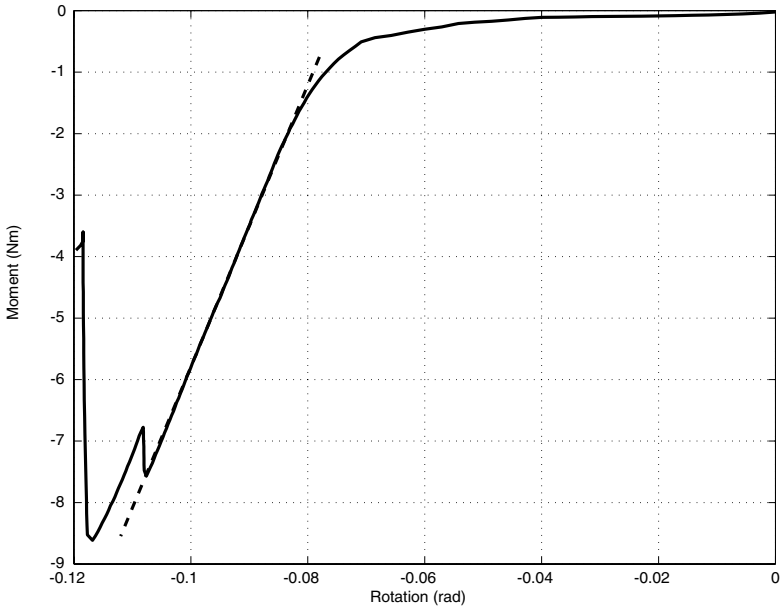

Figure 5.31: Tape-spring T_{yy} stiffness.

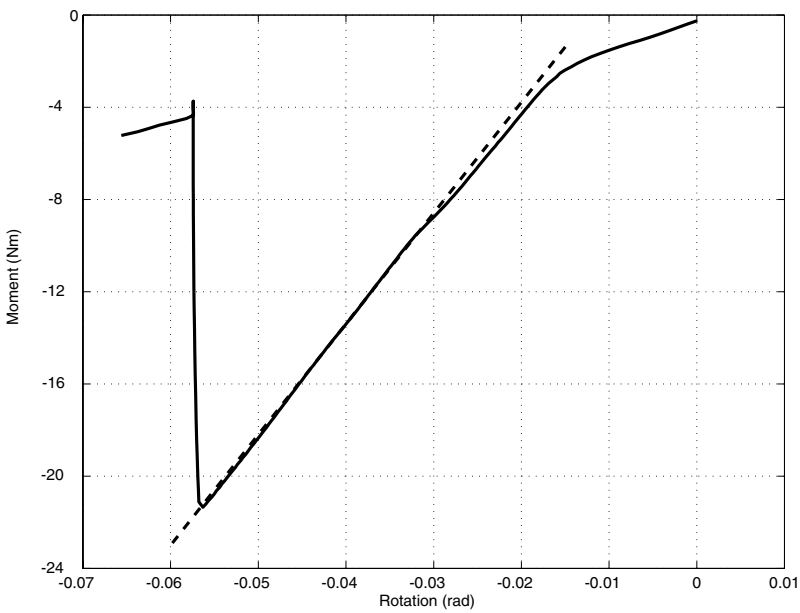

Figure 5.32: Total T_{yy} stiffness.

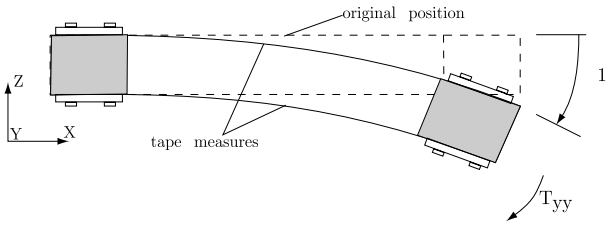

Figure 5.33: Definition of in-plane bending stiffness.

5.6 Out-of-Plane Bending Stiffness

The out-of-plane bending stiffness, T_{zz}, is the stiffness of the hinge bending around the z-axis.

Experimental Values

The stiffness of the Rolamite, tape-spring and total hinge were found with a four-point bending test setup, as shown in Figure 5.34. The results of these tests can be seen in Figures 5.35 to 5.37.

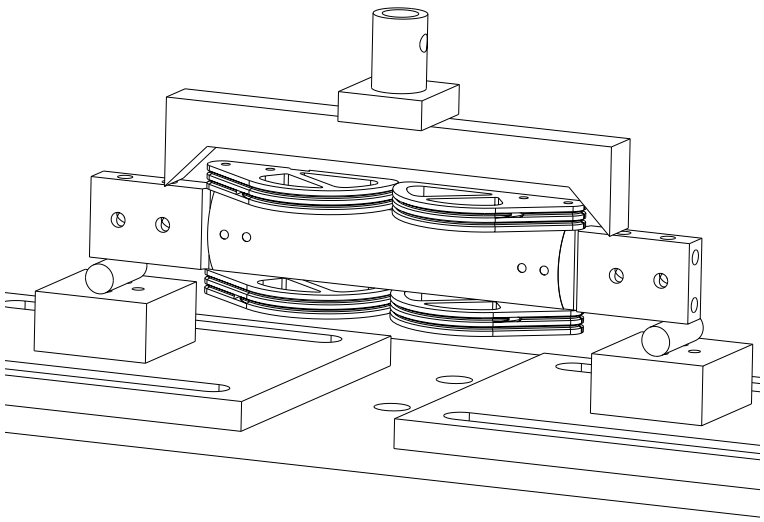

Figure 5.34: T_{zz} test set-up.

Prediction of Rolamite Stiffness

The Rolamite stiffness T_{zz} can be found from the same method used to find T_{xx}, which gives

$$T_{zz} = \frac{K_{xx}\ w^2}{2} \tag{5.19}$$

Using the previously predicted value of $K_{xx} = 1200$ N/mm and $w = 35$ mm gives $T_{zz} = 735$ Nm/rad, which compares to a measured value of 360 Nm/rad.

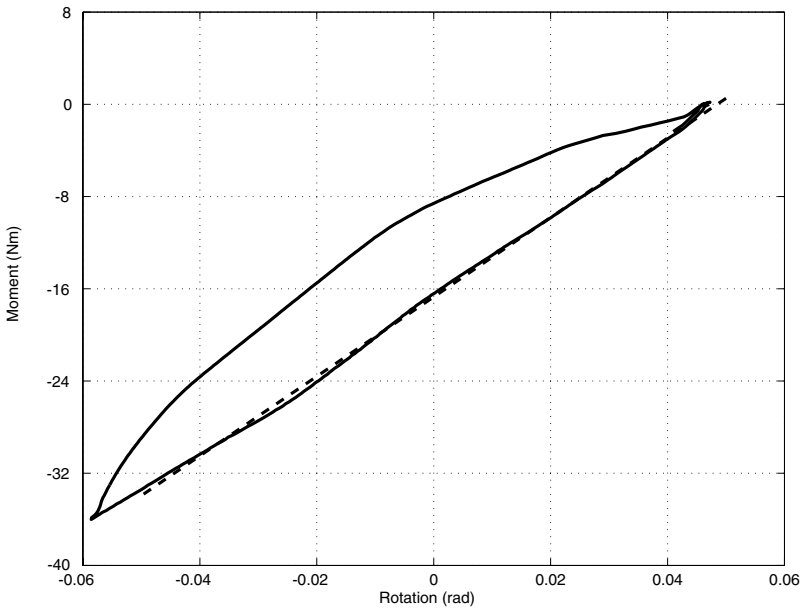

Figure 5.35: T_{zz} Rolamite stiffness.

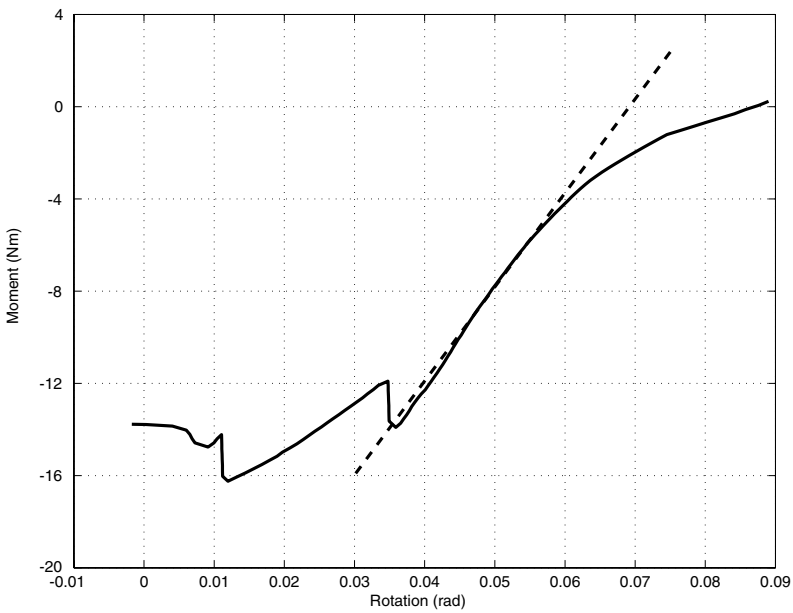

Figure 5.36: T_{zz} tape-spring stiffness.

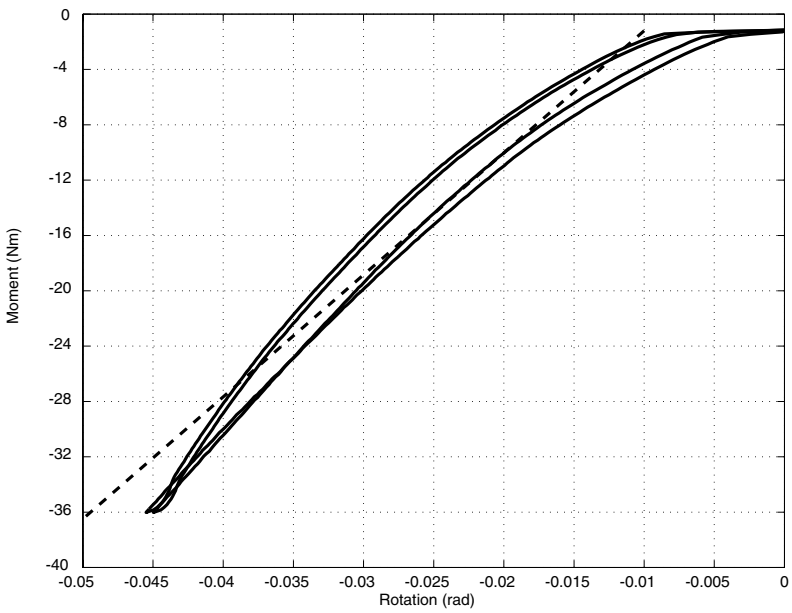

Figure 5.37: Total T_{zz} stiffness.

Prediction of Tape-Spring Stiffness

A simple expression for T_{zz} can be found by considering an encastre' beam, as defined in Figure 5.38

$$T_{zz} = 2\frac{EI_{zz}}{L} \tag{5.20}$$

For the properties given above this gives a stiffness of 451 Nm/rad, which compares with a measured value of 480 Nm/rad.

The ABAQUS model used in Section 5.1 was also used to predict the stiffness of the tape-spring. This model predicted a stiffness of 447 Nm/rad.

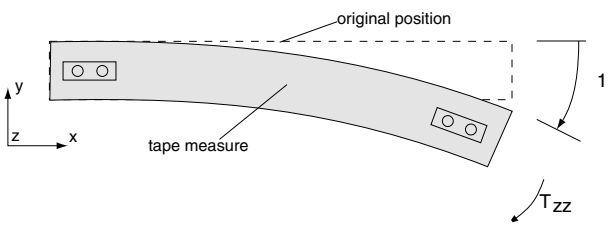

Figure 5.38: Definition of out-of-plane bending stiffness.

Total Stiffness

The total stiffness can again be found simply by adding the Rolamite and tape-spring contributions, as they are acting as springs in parallel. This gives a

predicted total stiffness of 1186 Nm/rad which compares to an experimental measurement of 782 Nm/rad.

The large difference between experimental and predicted results is due to poor predictions of both the Rolamite and tape-spring stiffnesses.

Chapter 6

Stowed Stiffness

No experimental measurements of the stowed stiffness of TSR hinges were taken. Measuring the linear stiffnesses should be fairly straightforward, however tests on the torsional and bending stiffnesses would be quite complex to arrange.

The stowed stiffnesses are dominated by the Rolamite hinge, as a tape-spring has very low stiffness in the stowed state. The predictions of the stiffness of the Rolamite hinge in the deployed configuration, in the previous chapter, were found to be reasonably accurate and it is assumed that equivalent predictions for the Rolamite stiffness in the stowed state (and hence overall stiffness) will be equally accurate.

The fact that the stowed stiffness is dominated by the Rolamite portion of the hinge, whereas most of the deployed stiffness arises from the tape springs, is thought to be a useful feature of these hinges. It would make it possible to tune the hinge design to give the required high deployed stiffness and low stowed stiffness. Stiffness predictions are also more reliable when the Rolamite only is considered.

A summary of the stiffness predictions for the stowed TSR hinge can be seen in Table 6.1. No practical measurements or predictions for the torsional or bending stiffness have been made.

Direction	Tapes	Rolamite	**TSR**	Units
K_{xx}	0	396	**396**	N/mm
K_{yy}	0	96	**96**	N/mm
K_{zz}	0	444	**444**	N/mm

Table 6.1: Summary of folded stiffness predictions.

6.1 Axial Stiffness

The axial stiffness K_{xx} of the hinge was predicted using a Pro/Mechanica finite element model of one side of the Rolamite hinge. This can be seen in Figure 6.2 and comprises 2940 "tetra" elements. This model predicted $K_{xx} = 336$ N/mm.

This model assumes the Rolamite parts of the hinge to be solidly connected together and ignores any loss of stiffness that could arise from the connections

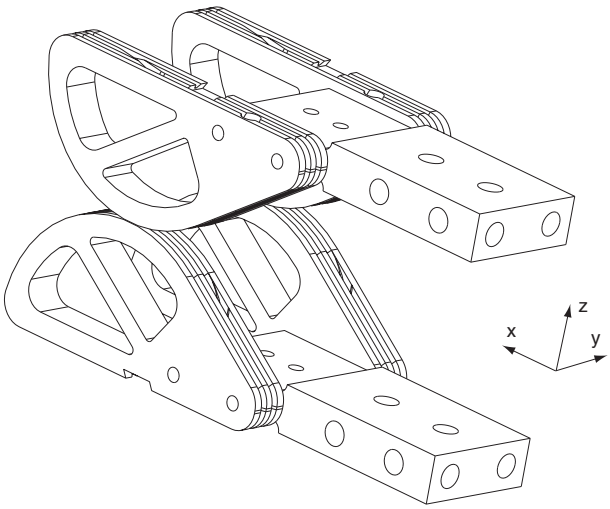

Figure 6.1: Definition of coordinate system for stowed hinge.

by the wires. Its stiffness prediction will therefore be likely to be an overestimate of the actual stiffness, but as these stiffness values are typically used to predict the maximum forces transmitted by the hinges during launch, this will lead to a conservative design.

In the previous chapter simple analytical models to estimate the deployed stiffness have been proposed. An equivalent beam model for the stowed hinge consists of a vertical beam that is fully encastre' and is deflected through a horizontal distance, see Figure 6.3. Its stiffness is then given by

$$K_{xx} = 2\frac{12EI}{L^3} \tag{6.1}$$

Using $E = 3.1$ kN/mm^2 for Delrin, for each side of the hinge $I = 666$ mm^4, and $L = 50$ mm gives $K_{xx} = 396$ N/mm

6.2 In-Plane Shear Stiffness

The Pro/Mechanica model used to find the axial stiffness was modified to find K_{yy}. This predicted a stiffness of 112 N/mm. Utilising the same analytical solution but this time with $L = 70$ mm and $I = 426$ mm^4 results in $K_{yy} =$ 96 mm.

6.3 Out-of-Plane Shear Stiffness

The Pro/Mechanica model used to find the extensional stiffness was modified to find the K_{zz} shear stiffness. This predicted a stiffness of 444 N/mm.

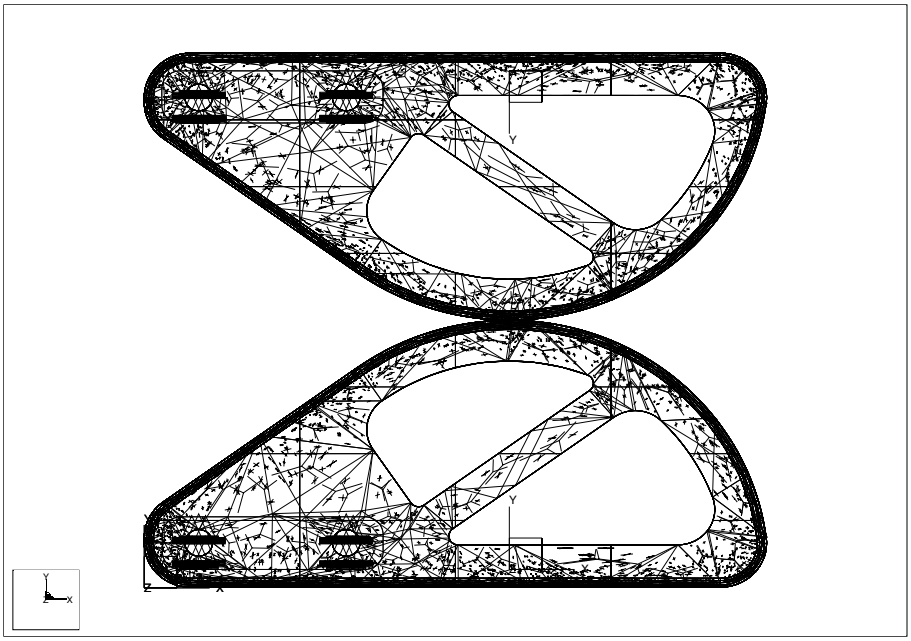

Figure 6.2: Pro/Mechanica model of stowed hinge.

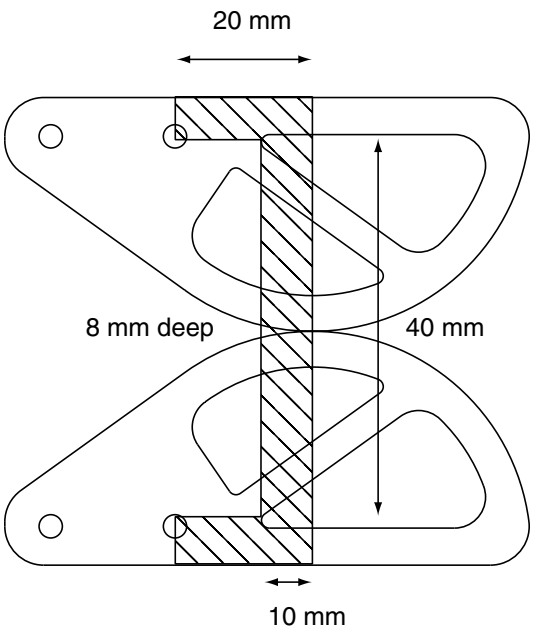

Figure 6.3: Stowed hinge equivalent beam model.

Chapter 7

Deployment of Honeycomb Panel

A mock-up of a deployable panel system on a satellite was made. It consists of two Al-alloy honeycomb panels, one fixed to a stiff, vertical support —representing the satellite bus— and the second, deployable, connected to the first by two TSR hinges version 2. This structure can be seen in Figure 7.1. Detailed drawings of the hinge connections, hinges and panels can be seen in Appendix a. The materials used are listed in Table 7.1.

Part	Material	Density (kg/m^3)
Hinge connections	Aluminium Alloy	2700
Hinge wheels	Delrin	1000
M4 Bolts	Steel	7800
Tape Springs	Spring Steel	7800
Panels	Aluminium Honeycomb	110

Table 7.1: Materials list.

7.1 Damping Methods

Deployment tests of the panel system were conducted for a number of different damping configurations on the hinge, as follows.

- No damping.
- Single layer of 3M 434 sound damping tape, applied to both sides of each tape spring as shown in Figure 7.2.
- Two brown Oasis foam blocks placed between the panels, as shown in Figure 7.3, to absorb the kinetic energy of the deploying panel prior to the hinge locking. The method for choosing the size of these blocks is described next.

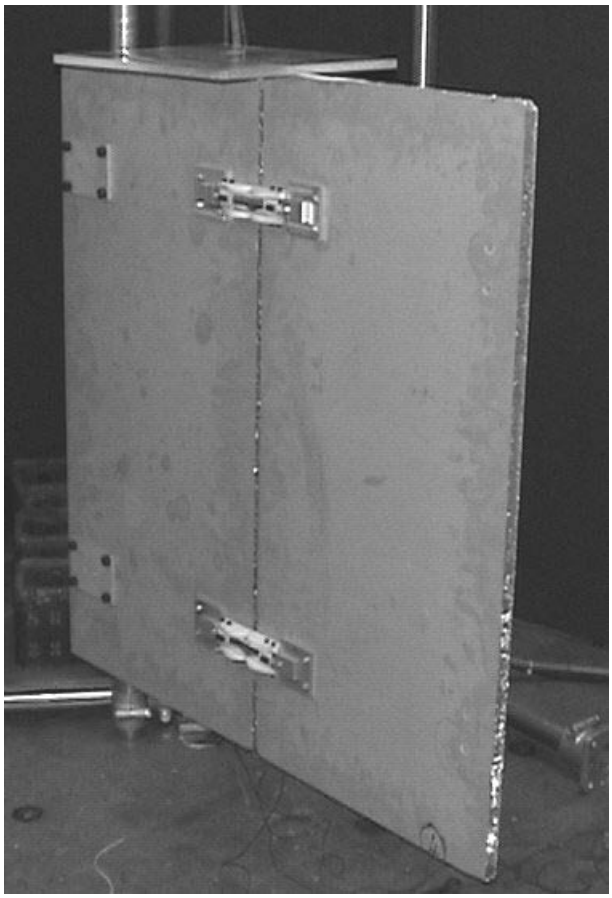

Figure 7.1: Deployable panel test set-up.

Figure 7.2: Damping tape on hinge.

Figure 7.3: Damping foam on panel.

7.1.1 Choice of Foam size

The size of the foam pads required to damp the panel was chosen by considering the energy that the foam has to remove from the system. This was initially found from integrating the area under the moment rotation graph, obtained from ABAQUS. However, it was considered more accurate to use the rotation vs time graph from the experiment to find the velocity and use this along with the known mass properties of the system to find the kinetic energy e. This was found to be 360 J (c.f. 494 J from integrating under the area of the moment rotation graph). Then, considering the foam block to be of length l_0 when crushed and have a constant crushing stress, σ_f, (0.14 N/mm^2 for brown Oasis foam) and choosing the total cross-sectional area, A, the required initial length of the foam, l can be found from

$$l = \frac{e}{2\sigma_f A} + l_0 \tag{7.1}$$

Assuming 2 blocks of width 50 mm, breadth 25 mm and crushed length 11 mm the length required was found to be 12 mm.

7.1.2 Shape Memory Foam

A shape memory foam block (Tobushi et al. 1996) could be used instead of standard foam blocks. This obviates two problems encountered with the use of crushable foam damping; the negative force and the lack of resettability.

A shape memory foam damping system would slow the hinge whilst in the low temperature, glassy state, providing a compressive, resisting force as the standard foam. Once the hinge has slowed down, the shape memory foam would be heated (by internal or external methods) and would then become plastic and

thus exhibit a significantly lower stiffness. The low stiffness would lower the resisting force applied by the foam, making the deploying force positive again and allowing guaranteed full deployment.

After use, the panel could be refolded and the foam reheated, thus resetting it to its original size.

7.2 Deployment Tests

The deployment of the panel was recorded using a Kodak EKTAPRO HS 4540 high speed video camera set at 250 frames per second. A rotation vs. time graph was constructed by recording when lines drawn on the deploying panel became aligned with angled lines printed on a perspex panel attached to the base panel. A typical picture captured by the high speed camera can be seen in Figure 7.4.

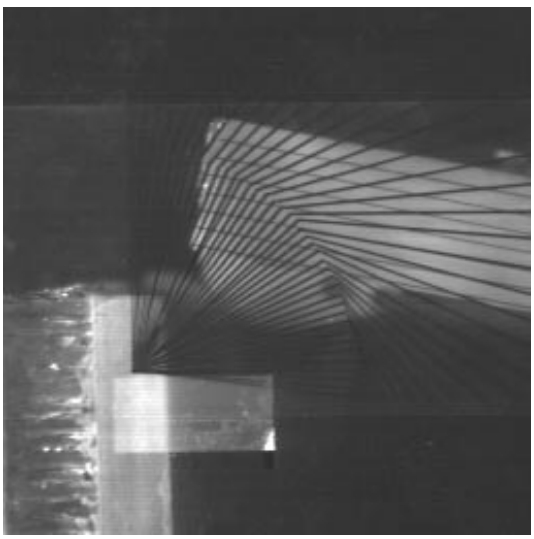

Figure 7.4: Typical high speed camera photo.

The results can be seen in Figure 7.5 for the undamped and damped case. If foam blocks are used, exactly the same results as the undamped case are obtained as the foam does not affect the large-scale rotation of the panel.

It can be seen that in both cases the hinges locked into position and that the damping caused a negligible difference in the rotation vs. time relationship.

7.3 Modelling of Deployment

A model of the deployment of the panel was made using Pro/Mechanica Motion (Parametric Technology Corp., 2001), a rigid body dynamic analysis program. This was considered to be much faster than producing a purely analytical model of deployment, as all of the parts had been designed within Pro/Engineer and could then be imported to Pro/Mechanica seamlessly. This model takes into account the complex geometry of the various parts and their different materials,

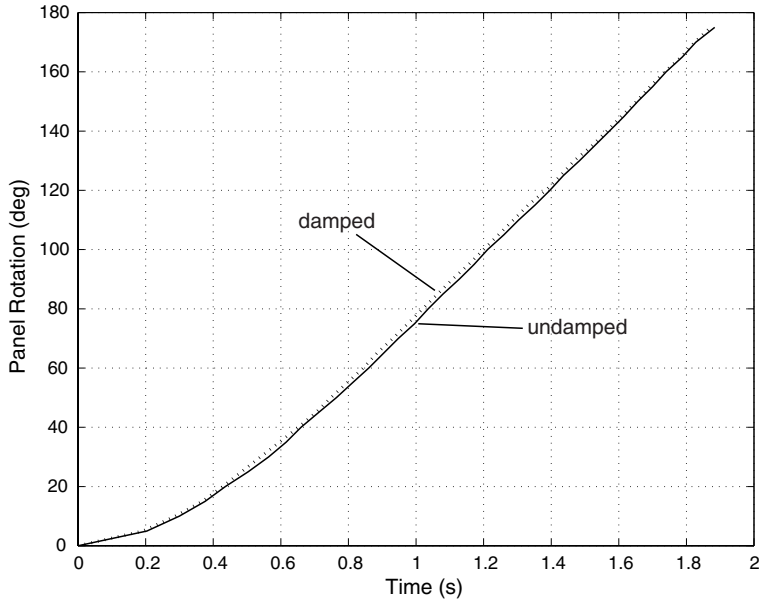

Figure 7.5: Panel rotation vs. time for damped and undamped hinges.

and finds the mass, centre of gravity and moments of inertia of the panels and hinges.

In order to model the correct kinematics of the hinge, a massless connecting beam of the same length as the diameter of the rolling surface of the hinge was connected by pin-joints to the centres of rotation of the two sides of the hinge. A massless gear pair of the same radius as the rolling surface of the hinge was connected to the hinge in order to constrain the rotations at each of the pin-joints to be the same, as the Rolamite hinge does in practice. This mechanism can be seen in Figure 7.6.

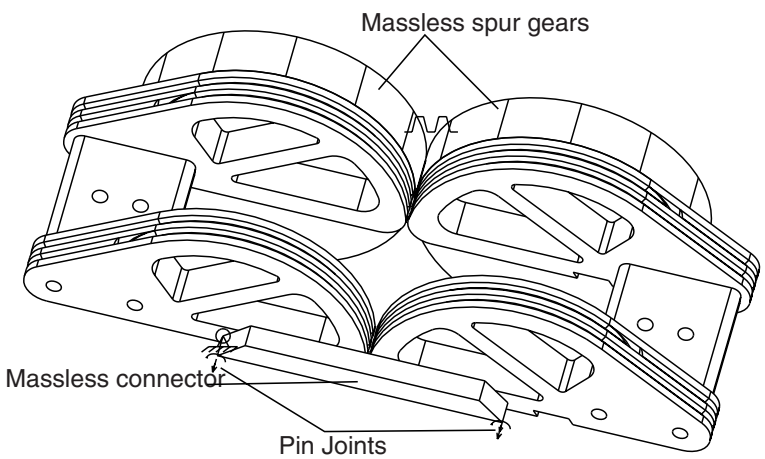

Figure 7.6: Pro/Mechanica dynamic model of hinge.

The loads applied to the model were those found from the folding and unfolding ABAQUS model of the version 2 TSR hinge. The ABAQUS moment-

rotation curves for this hinge can be seen in Figure 7.7 and 7.8. Note that here the rotation angle on the abscissa is defined to be zero in the initial, i.e. folded configuration.

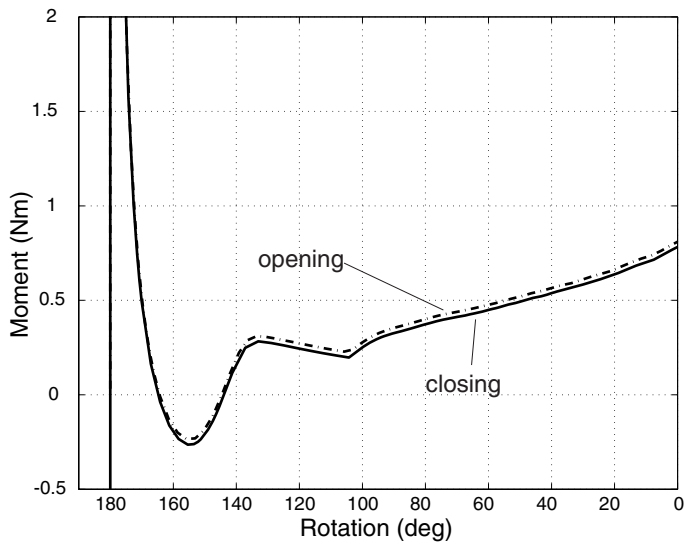

Figure 7.7: Opening and closing moments from ABAQUS (close-up).

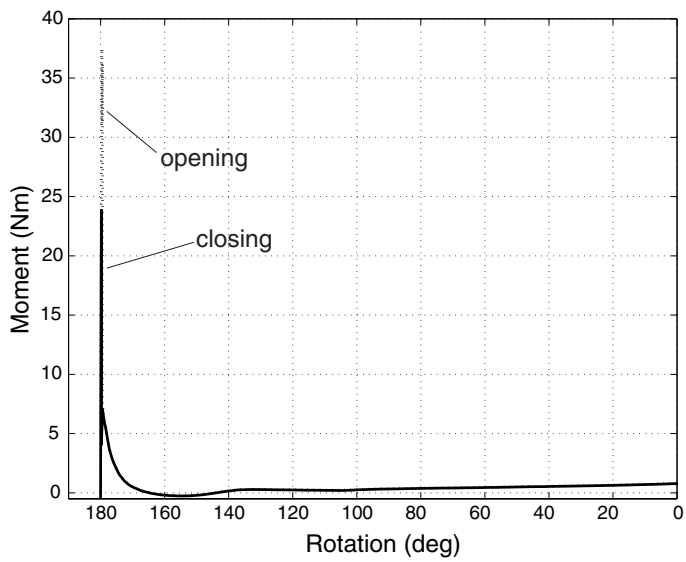

Figure 7.8: Opening and closing moments from ABAQUS (full-scale).

These loads were applied to the pin-joints on only one of the hinges and therefore were multiplied by two in order to take account of the fact that there are two hinges. The unfolding load was applied conditionally when the angular velocity of the hinge was greater than or equal to zero, whereas the folding loads were applied when the angular velocity became negative.

The rotation vs. time results from this model can be seen in Figure 7.9

along with the results from the undamped experimental test. It can be seen that the analytical results do not show the hinge locking but rather unlocking and rotating back to a rotation of around 20° and then oscillating backwards and forwards a number of times, before locking.

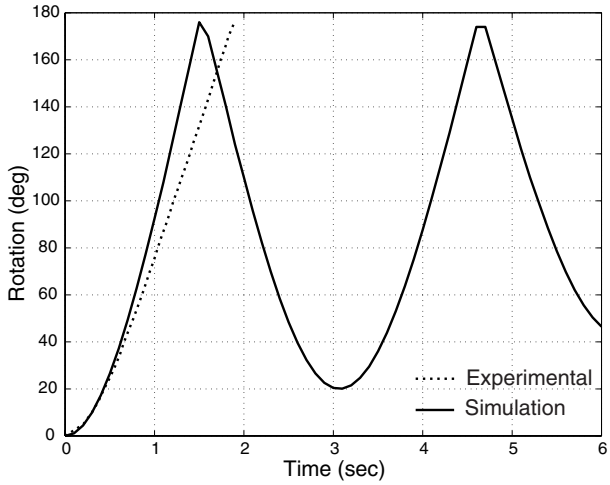

Figure 7.9: Comparison of Pro/Mechanica results with experiments.

The differences between the experimental and analytical results could be due to a number of factors:

- Damping within the hinge. Locking dissipates energy, due to stretching of the wires, compression of the hinge wheels, stretching of the tapes or slipping of the connections.
- Energy loss due to buckling of the tape springs.
- Incorrect modelling of the moment-rotation properties of the hinge where the moment-rotation properties of the hinge vary from those predicted by the ABAQUS analysis.
- Resistance during panel deployment. This resistance could arise due to friction within the hinge or air resistance on the panel.

The air resistance on the panel is the easiest of these effects to include within the model. According to BS 5400 Part 2 the drag force on a square panel can be found from

$$F = cdA\frac{\rho u^2}{2} \tag{7.2}$$

where F is the drag force, cd the drag coefficient, A the area of the panel, ρ the density of air, and u the velocity of the panel.

For a panel rotating at an angular velocity ω around a fixed point, the velocity of a point on the panel at distance x from the hinge is

$$v = \omega x \tag{7.3}$$

The velocity of the panel supported by tape-spring hinges can be obtained from the same equation, although if the angular velocity of one of the Rolamite wheels, ω_h, is the reference variable in the Pro/Mechanica model it should be doubled to give the equivalent ω, hence

$$v = 2\omega_h x \tag{7.4}$$

The overall force on a panel of height h and length l can then be found by integrating over the whole panel

$$F = \int_0^l \frac{cd\rho\omega_h^2 x^2 h}{8} dx = \left[\frac{cd\rho\omega_h^2 x^3 h}{24}\right]_0^l \tag{7.5}$$

This force acts at a distance of $2^{-1/3}\ l$, i.e. 0.7937 l along the panel. Such a force was added to the Pro/Mechanica model using $\rho = 1.223$ kg/m^3, the panel height of 1 m and width of 0.5 m and $cd_{max} = 2.8$ as recommended in BS 5400. The results can be seen in Figure 7.10 along with the results not including air resistance and the experimental results.

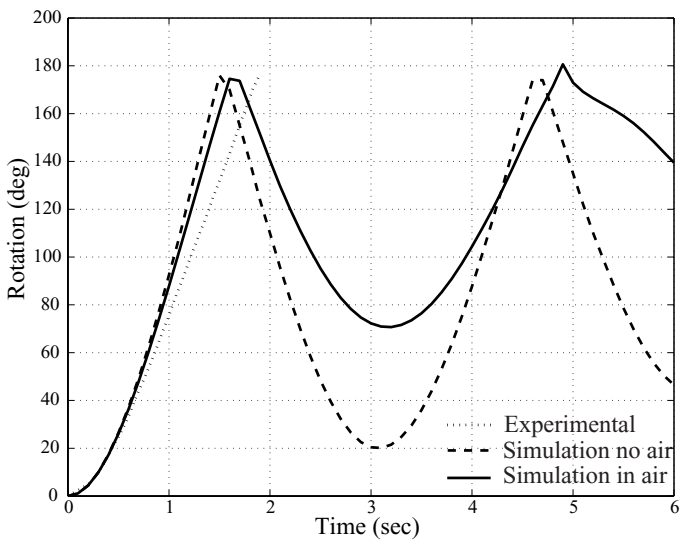

Figure 7.10: Pro/Mechanica rotation vs time results including air damping.

7.4 Shock Measurements

In addition to measuring the rotation of the panels, four accelerometers were attached, two to the base panel and two to the moving panel in the positions shown in Figure 7.11. These positions and orientations were chosen so that the angular and radial accelerations of the two panels due to the shock imparted by the hinges could be measured. The distance from the hinge attachment to the accelerometer position was minimised so as to reduce any energy dissipation. The accelerometer output was logged using a National Instruments analogue to

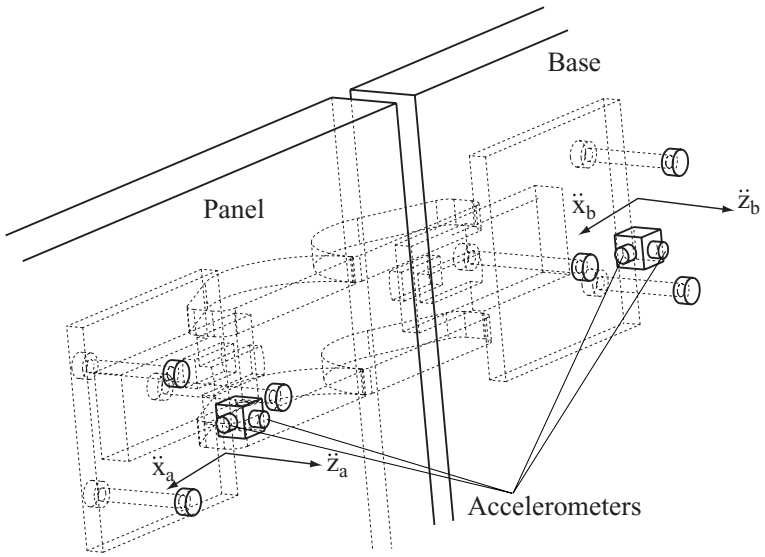

Figure 7.11: Accelerometer positioning.

digital conversion board and a program written in Labview (National Instruments, 1998). The logging rate was set at 5000 logs per second.

The shock resulting from deployment of a panel with no damping in the hinges can be seen in Figure 7.12. It can be seen that the hinge does not lock fully on deployment but rather re-buckles twice creating a total of three impulses. It can be seen that the maximum acceleration applied is approximately 1500 m/s^2 (150 g).

The shock resulting from deployment of a panel with a 12 mm long piece of Oasis foam can be seen in Figure 7.13. It can be seen that the panel now locks the first time, without re-buckling the tape-springs, and that the maximum acceleration is now reduced to approximately 600 m/s^2. The successful deployment of the panel was very sensitive to the length of the foam block used. For example, if a 12.5 mm piece of foam was used, the panel would not lock, but would remain at around 5° from the straight position.

It should be noted that in order for this damping system to work, kinetic energy is removed from the system. This requires the foam to apply a larger closing force to the panel than the opening force applied by the hinge.

The foam damping system might face verification difficulties due to the fact that it is a single use, unresettable system. This would make reliability and repeatability testing problematic. Therefore, shape-memory foam may be preferable.

The shock resulting from the deployment of a panel with 3M 434 sound damping tape attached to both sides of each tape-spring can be seen in Figure 7.14. It can be seen that the maximum shock is now around 250 m/s^2. However the post-locking vibration is still present. This method of damping a tape-spring is covered by a patent (Dupperray et al., 2001).

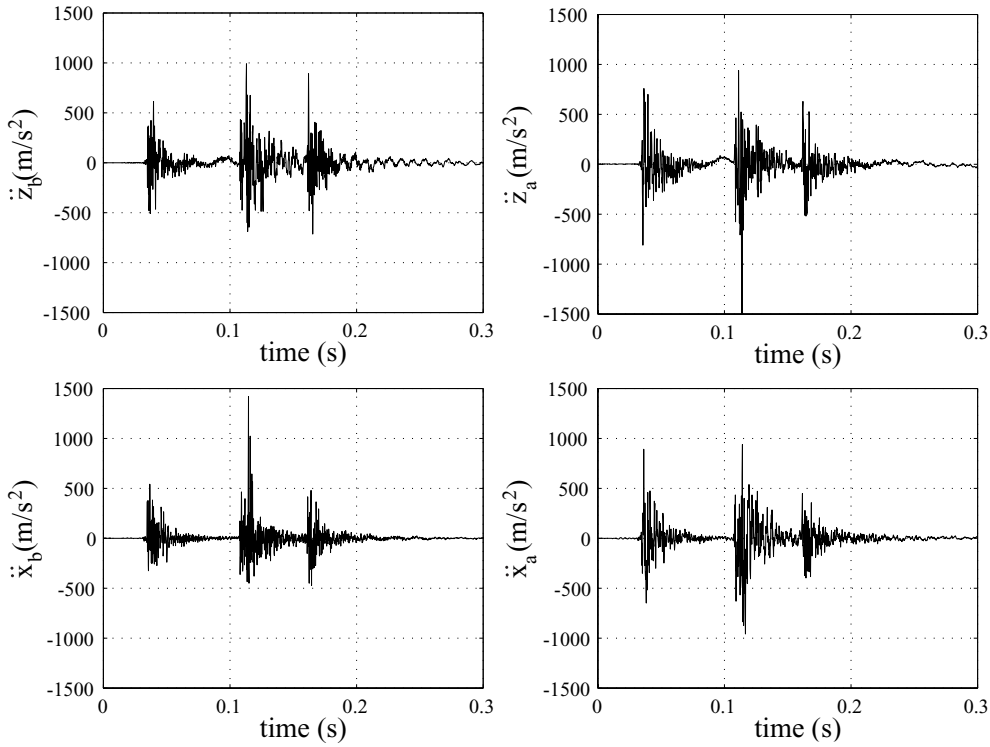

Figure 7.12: Locking shock for panel with no damping.

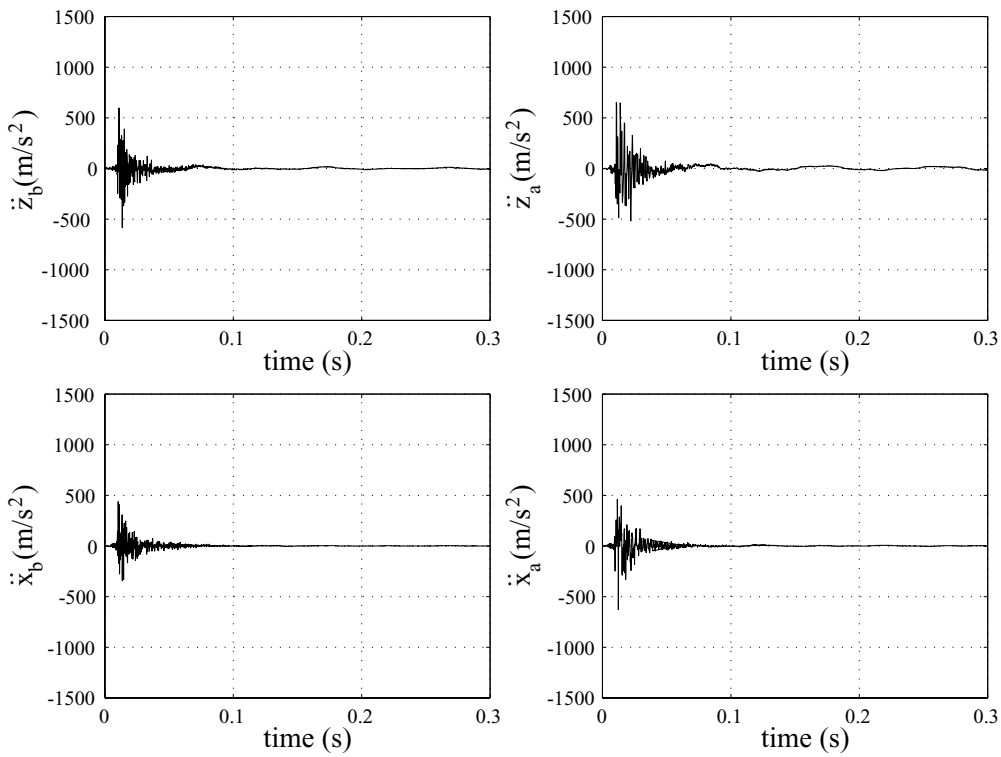

Figure 7.13: Locking shock for panel with 12 mm long brown Oasis foam blocks.

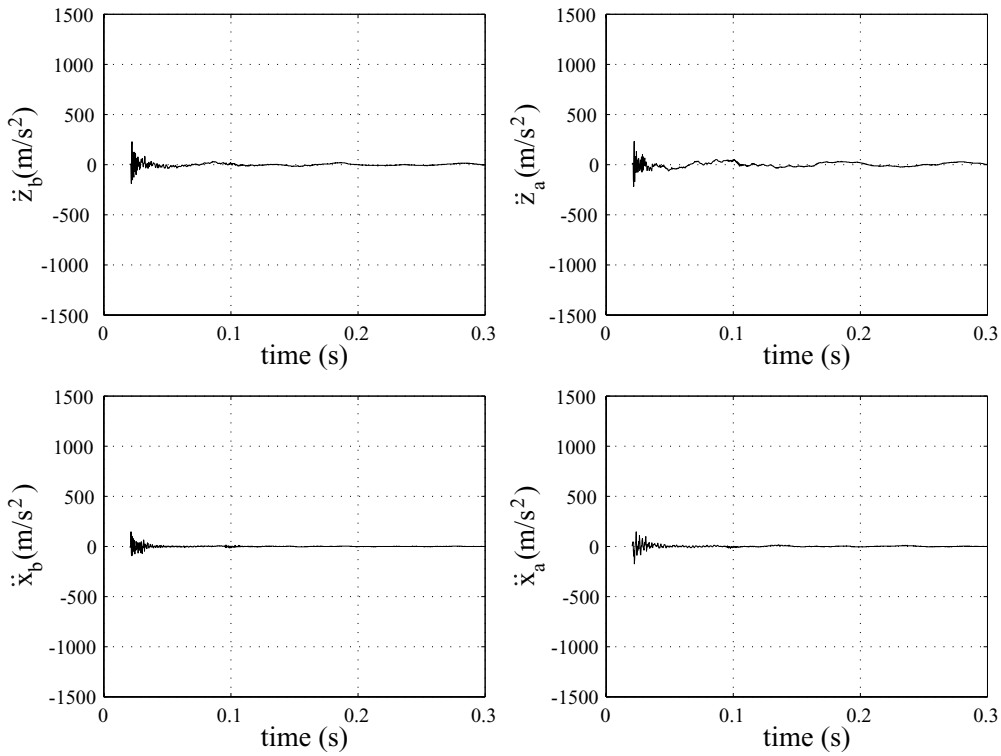

Figure 7.14: Locking shock for panel with 3M 434 sound damping tape.

7.5 Alternative Damping Methods

A number of other methods for damping TSR hinges have been considered.

7.5.1 Fluid-filled Deformable Tube

This damping system would consist of sealed fluid-filled tubes wrapped around the Rolamite body of the hinge. Where the Rolamite wheels come into contact the tube would be flattened; then, as the hinge rotates, the flattened portion of the tube would move around the radius of the hinge and the fluid would be forced around the tube. The flow of the fluid would be restricted by a small orifice. A schematic diagram of such a system can be seen in Figure 7.15.

The flow rate, Q, through an orifice varies with the pressure difference across the orifice, Δp, the orifice area, A_0, and a constant k

$$Q = kA_0\sqrt{\frac{2\Delta p}{\rho}} \tag{7.6}$$

The value of k varies with the Reynolds number and the orifice diameter divided by the pipe diameter, d/D. The value of k is plotted for various Reynolds numbers and diameters in Roberson and Crowe (1976), however for values of d/D of less than 0.1 (as is likely to be the case for the orifice being considered) $k \approx 0.6$.

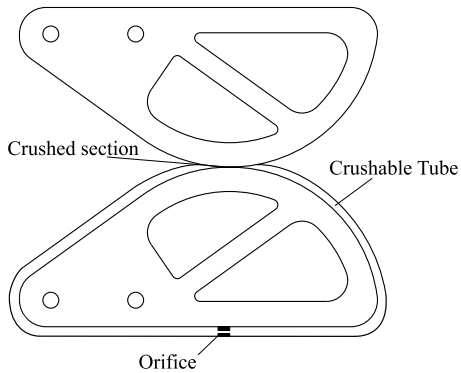

Figure 7.15: Crushable tube damping system.

The resisting moment, M, provided by the crushable-tube damping is proportional to the pressure difference, ΔP and can be found from

$$M = \Delta p A_1 R \tag{7.7}$$

The angular velocity, ω, of the hinge can be found from the flow rate

$$\omega = \frac{Q}{A_1 R} \tag{7.8}$$

Rearranging Equations 7.6 to 7.8 gives a relationship between the angular velocity of the hinge and the resistive moment

$$A_0 = \frac{A_1 \omega}{k} \sqrt{\frac{\rho A_1 R^3}{2M}} \tag{7.9}$$

For a deployment time of the order of seconds, fluids of specific gravity of around 1, moment resistance of 0.2 Nm and pipe inside diameters of 5 mm, A_0 can be found to be 3×10^{-5} mm^2. This gives a hole diameter of 0.03 mm. Such a small diameter would be difficult to manufacture and also clogging is likely to be a problem. The diameter could be slightly increased while making the orifice longer, and thus increasing friction effects. This, however, does not make a huge difference on the diameter resulting from the calculation.

There would be potential qualification problems for such a system, due to the use of a fluid in an elastic tube that is subject to high strain levels.

7.5.2 Sorbothane Dampers

Shock reduction could be achieved by attaching the hinges to the panels through Sorbothane (Sorbothane, 2002) bushings. Sorbothane is a visco-elastic polymer that has a stable dynamic Young's Modulus over a wide temperature range.

Chapter 8

Conclusions

As discussed in Chapter 2, tape-spring hinges were invented in 1968 and rolling joints in 1976; a hinge combining tape-springs and rolling joints was invented in 1992. In comparison with these earlier designs, the TSR hinges presented in this report are significantly lighter and smaller. Also they are based on a modular approach, which makes it easy to re-configure them to change their properties with only minor design changes. For example, their deployment moment can be increased by a factor of two or three by using two or three overlapped pairs of tape springs, respectively.

Chapter 3 has introduced a finite-element modelling technique to simulate the complete moment-rotation relationship of a TSR hinge. Overall, experimental measurements agree closely with results from this simulation, see Figure 3.10 and Figure 3.11, but the combination of high stiffness and snap-through behaviour at small angles of rotation makes it difficult to track experimentally the equilibrium path of the hinge. Hence, although for a specific hinge design (version 2) the measured peak moment during *folding* of the hinge (locking moment) is predicted to a reasonable accuracy, i.e. over-estimated by 50%, during *deployment* the measured peak moment was less than 10% of the value predicted. It seems likely that compliance in the testing machine and in the Rolamite wheels and steel wires of the TSR hinge connecting them is responsible for this discrepancy.

A parametric study of the moment-rotation relationship of TSR hinges with fixed Rolamite radius $r = 28.1$ mm, tape spring length $L = 126$ mm and transverse radius $R_c = 15$ mm, but different values of the spacing s between the tape springs and the offset d between the tape springs and the Rolamite wheels has been presented in Chapter 4. During the course of this study the initial hinge design was improved to "version 2", which combines a high locking moment, in excess of 10 Nm, to an essentially non-negative moment during deployment (the predictions show a small negative moment for a small range of rotation angles, but this is not observed in practice). Further improvement of this design is possible, as it was later found that for $d = 8$ mm the moment-rotation relationship becomes non-negative.

Chapter 5 has presented an extensive experimental study of the deployed stiffness of the version 1 TSR hinge, i.e. not the improved version, from which

the three linear and three rotational stiffness coefficients of the hinge have been obtained. The range within which each stiffness coefficient can be assumed to remain constant has been identified, and the separate contributions made by the tape-springs and the Rolamite hinge have been measured. A simple analytical method for predicting these stiffnesses has been proposed and it has been shown to be reasonably accurate for design purposes.

Deployment tests have been carried out on a mock-up of a two-panel system for a spacecraft, consisting of Al-alloy sandwich panels connected by two TSR hinges version 2. A key aim of these tests was to evaluate different ways of providing damping during deployment and of reducing the shock levels during latch-up. Specifically, tests were conducted (i) without any damping materials, (ii) with damping tape attached to the surface of the tape springs, and (iii) with crushable foam pads mounted on the inside of the hinge. The outcome of these tests is as follows, first, the overall deployment time is the same in all three cases, second, the shock was reduced by a factor of about 3 with the foam pads and by a further factor about 2 with the damping tape. A deployment simulation, based on an ABAQUS generated moment-rotation relationship of the hinges incorporated in a Pro/Mechanica model of the panels, works well in predicting the overall deployment dynamics. However, predicting, or even just understanding the mechanism through which energy is dissipated within the hinge during latching is a topic where further work is needed.

References

Auternaud, J. et al. (1992). Self motorized antifriction joint and an articulated assembly, such as a satellite solar panel equipped with such joints, U.S. Patent 5,086,541. 11 February, 1992.

Chiappetta F.R., Frame C.L. and Johnson K.L. (1993). Hinge element and deployable structure including hinge element, U.S. Patent 5,239,793. August 31, 1993.

Chironis, N.P. and Sclater, N. (1996). Mechanisms and mechanical devices sourcebook. Second Edition, McGraw-Hill, New York.

Dupperray B., Donzier A. and Sicre J. (2001). Automotive, self-locking and damping articulated joint and articulation equipped with same, European Patent 0,939,727,B1. January, 2001.

Hibbit, Karlsson and Sorensen (2000). ABAQUS Version 6.1.0. Pawtucket, RI 02860.

Hilberry, B.M. and Hall, A.S. (1976). Rolling contact prosthetic knee koint, U.S. Patent 3,945,053. 23 March, 1976.

Johnson, K.L. (1987). *Contact Mechanics*, Cambridge University Press, Cambridge.

National Instruments (1998). Labview Version 5.0.1.

Parametric Technology Corporation (2001). Pro/Mechanica Motion 2001, 140 Kendrick St, Needham, MA 02494.

Pellegrino, S., Green, C., Guest, S.D. and Watt A. (2000). SAR Advanced Deployable Structure. CUED/D-STRUCT/TR191, Department of Engineering, University of Cambridge.

Roberson, J.A. and Crowe, C.T. (1975). *Engineering Fluid Mechanics*, Houghton Mifflin, Boston.

Seffen, K. A. and Pellegrino, S. (1999). Deployment dynamics of tape springs. Proceedings of the Royal Society of London, series A, **455**, 1003-1048. Sorbothane 2002, www.sorbothane.com, 2144 State Route 59 Kent, Ohio 44240

Tobushi, H., Hara, H., Yamada, E. and Hayashi, S. (1996). Thermomechanical properties of shape memory polymer of polyurethane series and their applications. In: *Proc. Third ICIM/ECSSM'96* Lyon, France, pp. 418-423 .

Vyvyan, W.W. (1968). Self-actuating, self-locking hinge, U.S. Patent 3,386,128. 4 June, 1968.

Wilkes, D.F. (1969). Roller-band devices, U.S. Patent 3,452,175. 24 June, 1969.

Appendix A

Hinge Drawings

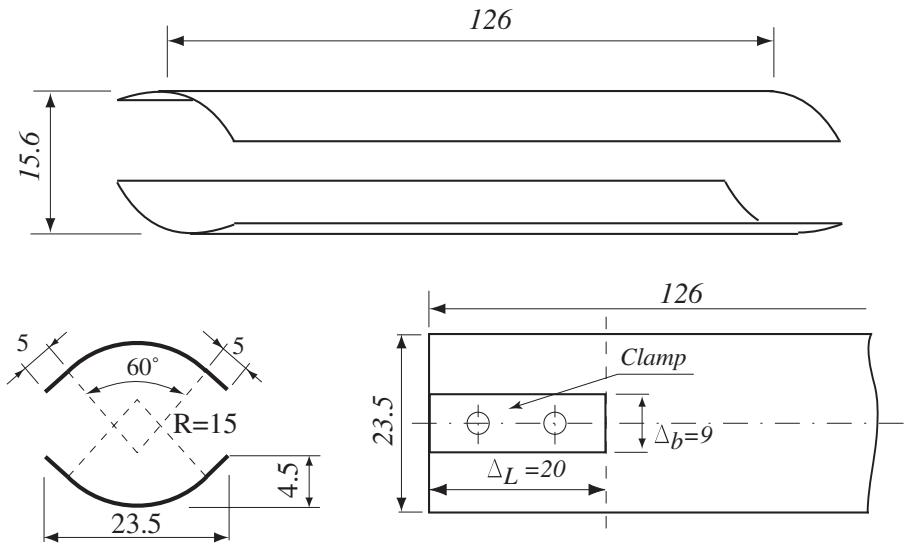

Figure A.1: Geometry of tapes, dimensions in mm.

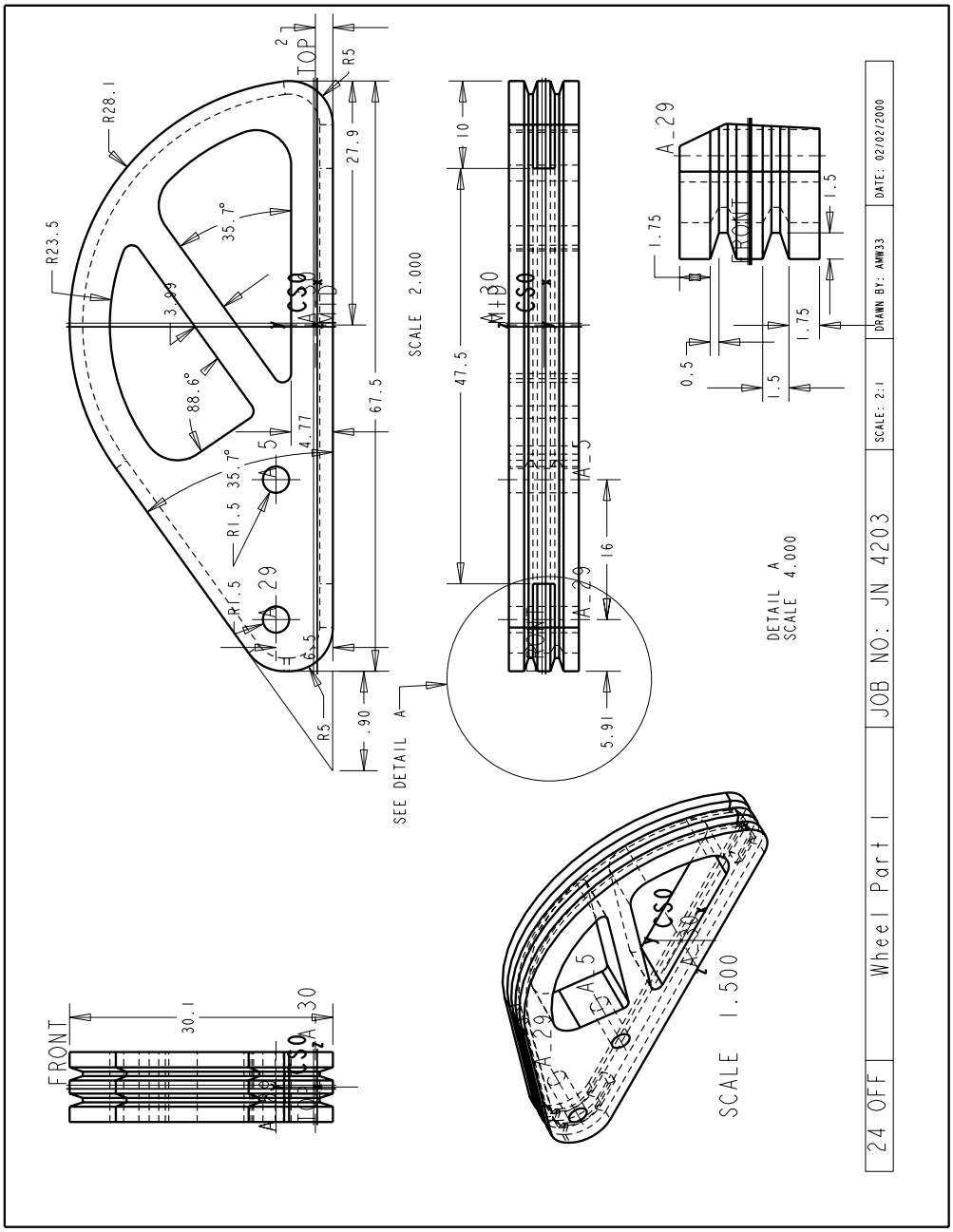

Figure A.2: Rolling contact pieces (hinge version 1).

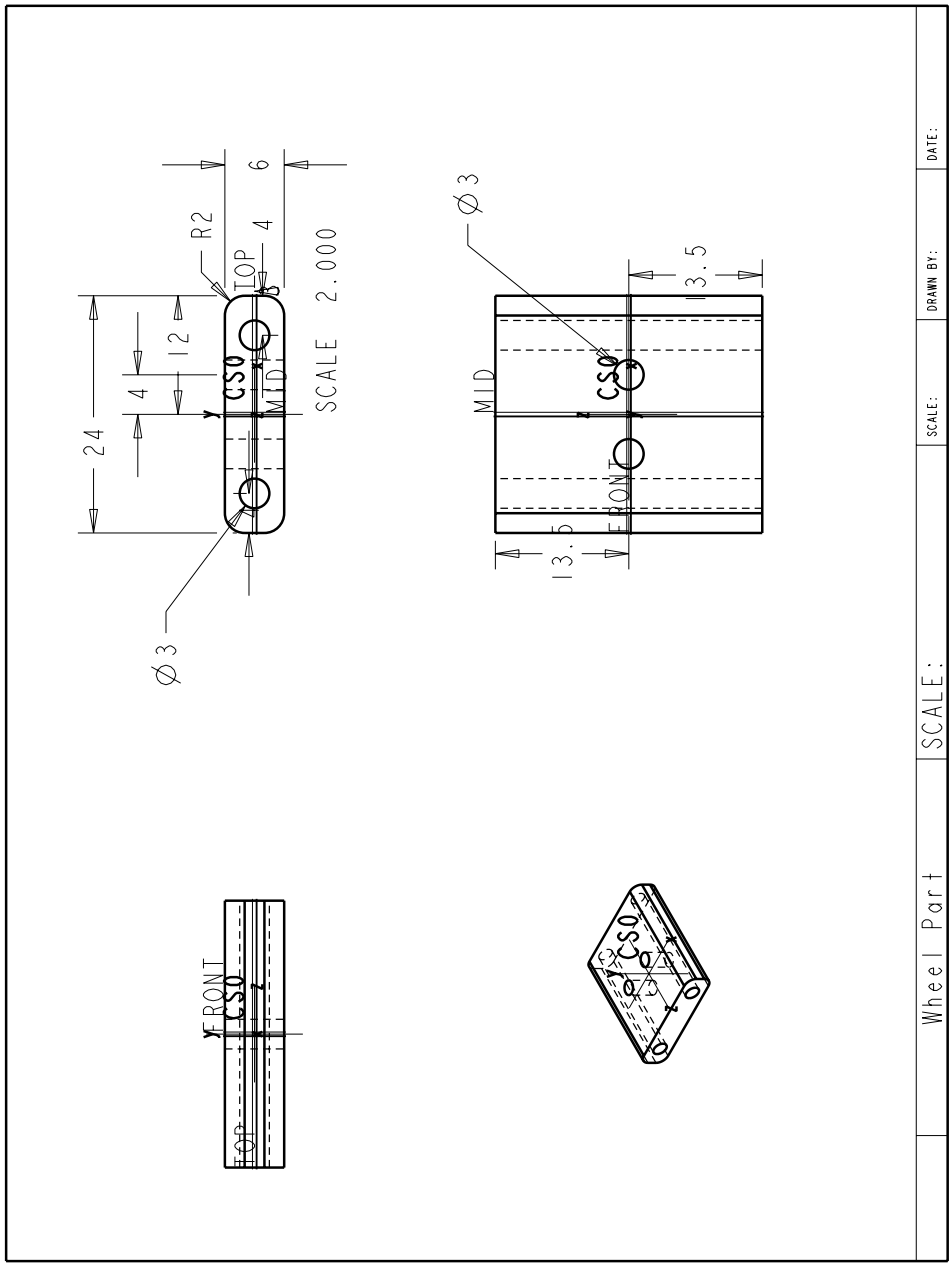

Figure A.3: Connection piece 1.

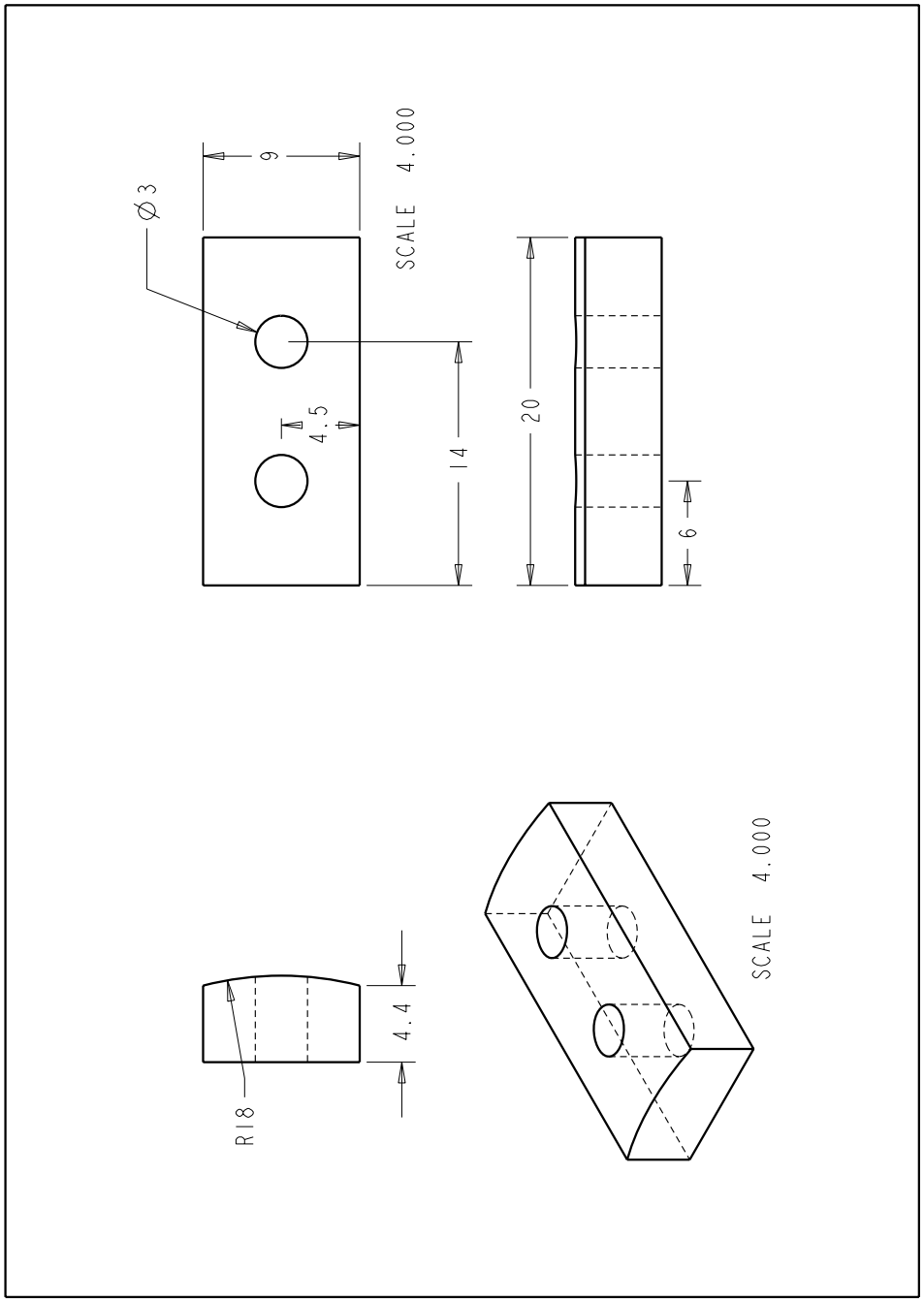

Figure A.4: Connection piece 2.

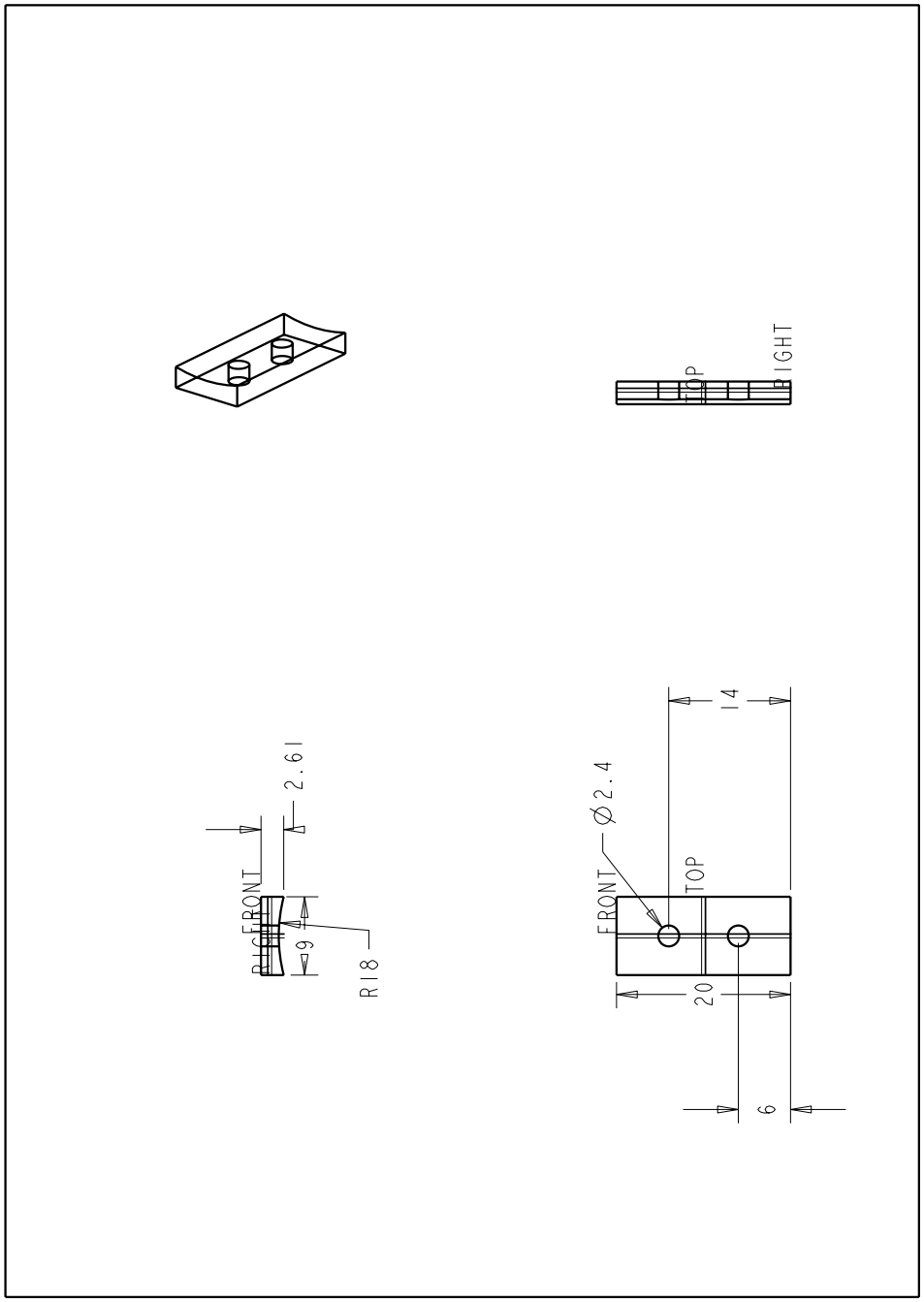

Figure A.5: Connection piece 3.

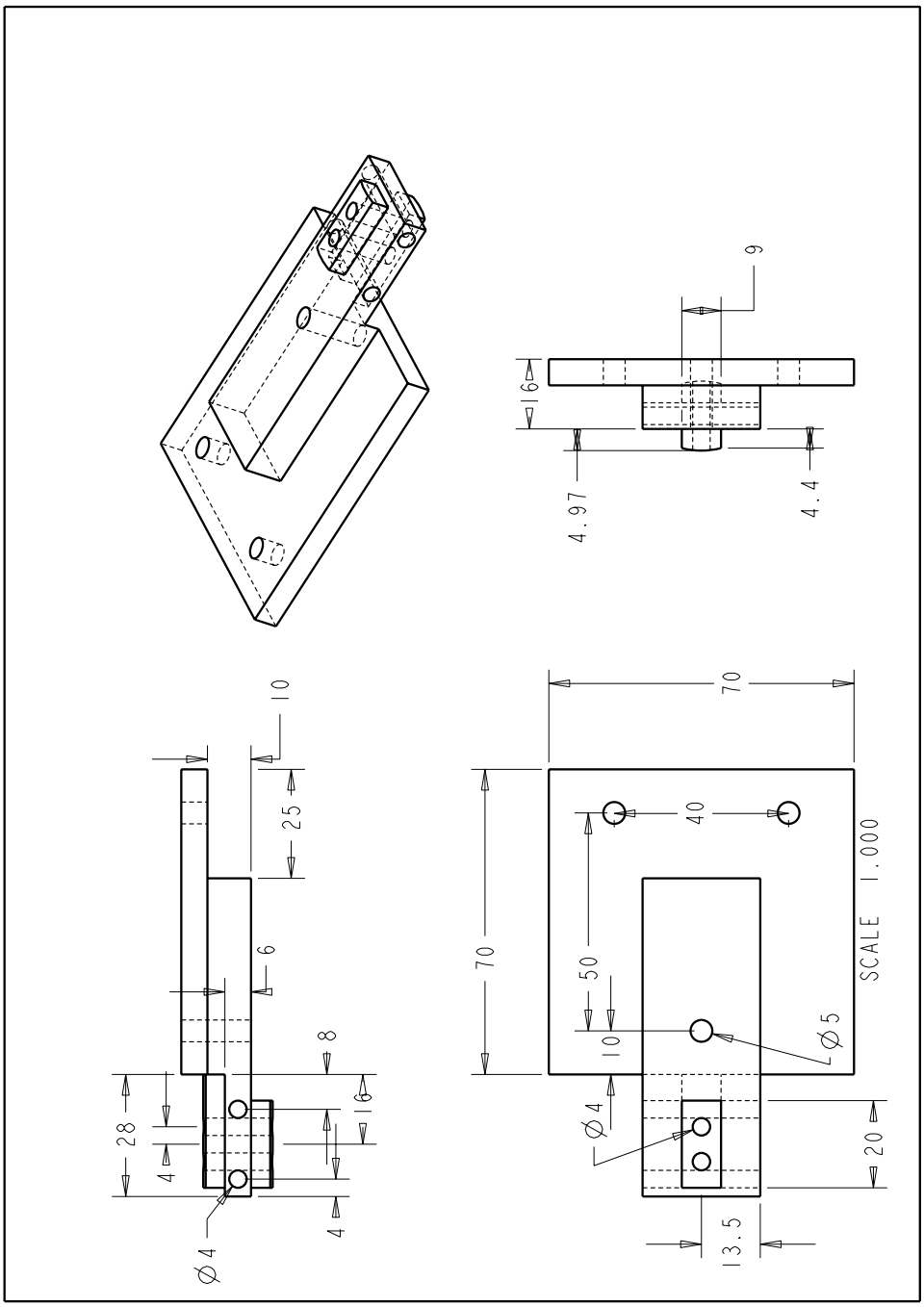

Figure A.6: Deployment panel connection piece.

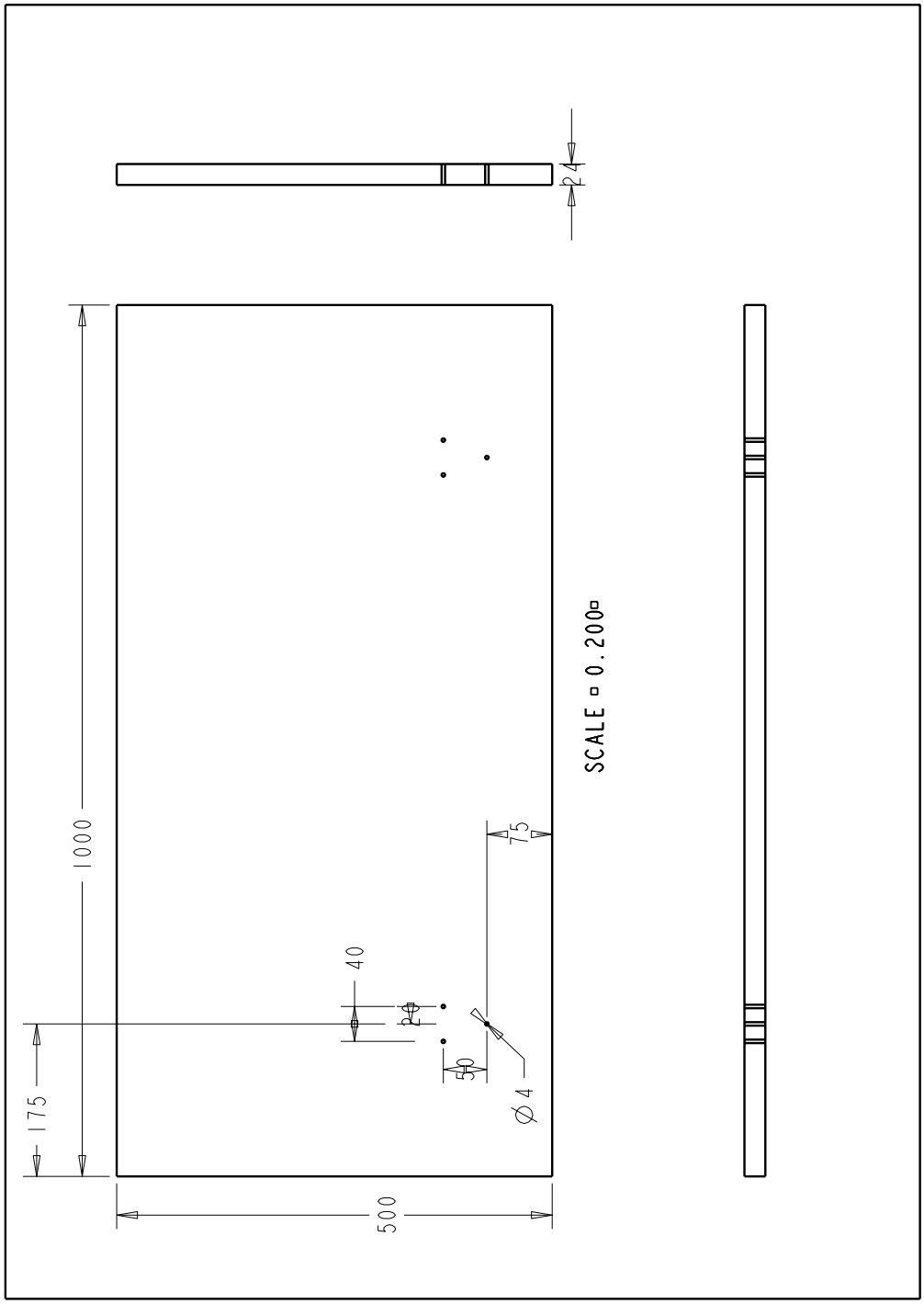

Figure A.7: Aluminium honeycomb deployment panel.

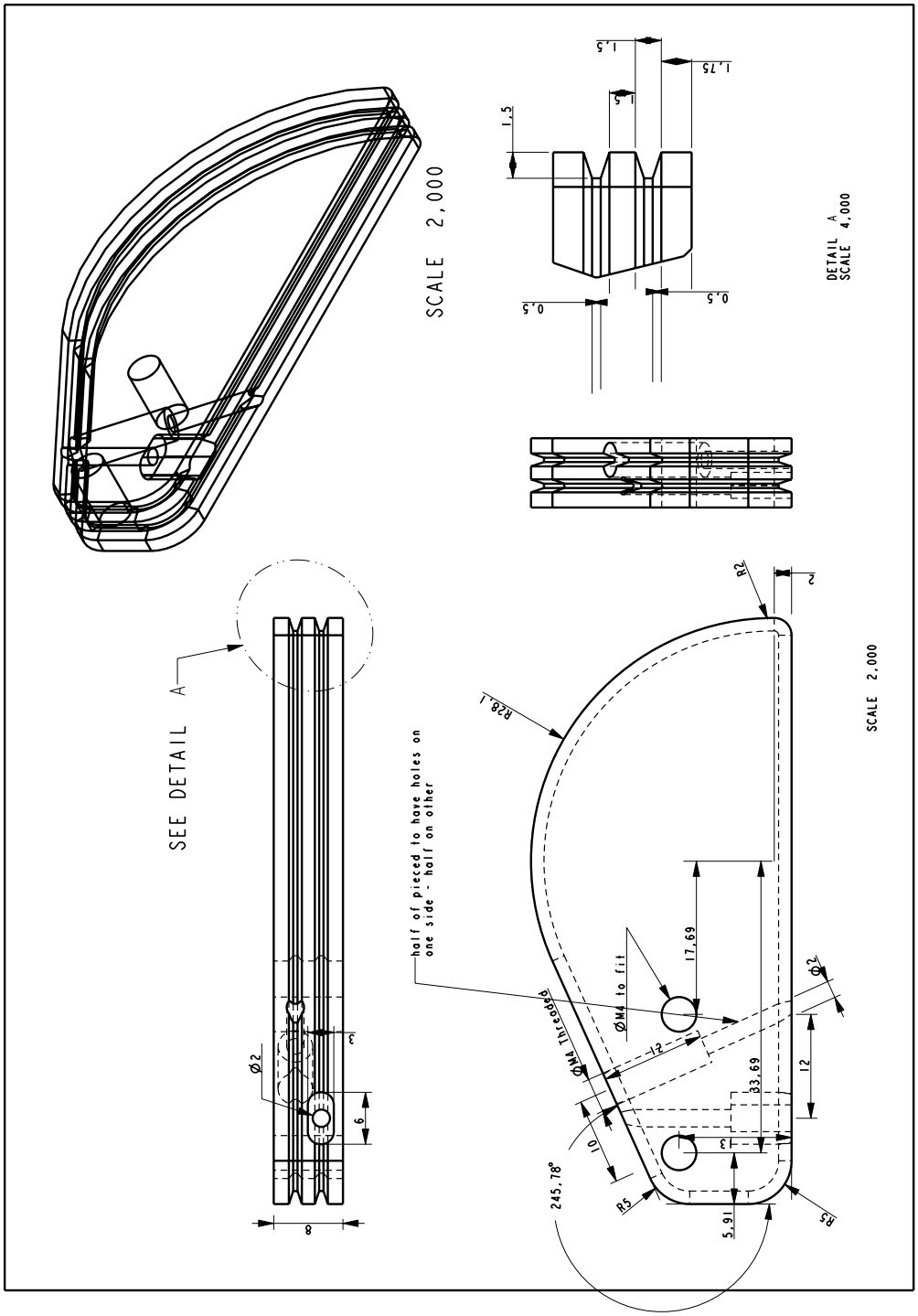

Figure A.8: Rolling contact piece (hinge version 2).

Appendix B

ABAQUS Input File

ABAQUS input file for tape hinge simulation

```
*HEADING
** TAPE HINGE ANALYSIS****************
*PREPRINT, ECHO=NO, HISTORY=NO, MODEL=NO
*************************************
** DEFINING THE NODES FOR THE TAPES **
*************************************
*NODE
1,-12.65,-63,3.2
2,-10.59,-63,4.35
...
1662,10.59,63,-4.35
1663,12.65,63,-3.2
*************************************
**       CREATING NODE SETS         **
*************************************
*NSET, NSET=TOP_FRONT, GENERATE
1,13,1
*NSET, NSET=TOP_BACK, GENERATE
651,663,1
*NSET, NSET=TOP_LEFT, GENERATE
1,651,13
*NSET, NSET=TOP_RIGHT, GENERATE
13,663,13
*NSET, NSET=BOTTOM_FRONT, GENERATE
1001,1013,1
*NSET, NSET=BOTTOM_BACK, GENERATE
1651,1663,1
*NSET, NSET=BOTTOM_LEFT, GENERATE
1001,1651,13
*NSET, NSET=BOTTOM_RIGHT, GENERATE
```

```
1013,1663,13
*NSET, NSET=TOP_TAPE_N, GENERATE
1,663,1
*NSET, NSET=BOTTOM_TAPE_N, GENERATE
1001,1663,1
*NSET, NSET=TAPES_N
TOP_TAPE_N,BOTTOM_TAPE_N
**************************************
**      CREATING SHELL ELEMENTS     **
**************************************
*ELEMENT, TYPE=S4
1, 1, 14, 15, 2
*ELGEN, ELSET=TOP_TAPE_EL
1, 12, 1, 1, 50, 13, 12
*ELEMENT, TYPE=S4
1001, 1001, 1014, 1015, 1002
*ELGEN, ELSET=BOTTOM_TAPE_EL
1001, 12, 1, 1, 50, 13, 12
*ELSET, ELSET=TAPES_EL
TOP_TAPE_EL,BOTTOM_TAPE_EL
**************************************
**  MATERIAL PROPERTIES FOR TAPES   **
**************************************
*MATERIAL, NAME=STEEL
*ELASTIC, TYPE=ISO
200000, 0.3
**************************************
**     SHELL SECTION DEFINITION     **
**************************************
*SHELL SECTION, ELSET=TOP_TAPE_EL, MATERIAL=STEEL
0.1, 5
*SHELL SECTION, ELSET=BOTTOM_TAPE_EL, MATERIAL=STEEL
0.1, 5
**************************************
**     NODES WITHIN THE CLAMPS      **
**************************************
*NSET, NSET=FRONT_CLAMP
5,18,31,44,6,19,32,45,7,20,33,46,8,21,34,47
9,22,35,48,1005,1018,1031,1044,1006,1019,1032,1045,1007,1020
1033,1046,1008,1021,1034,1047,1009,1022,1035,1048
*NSET, NSET=BACK_CLAMP
616,629,642,655,617,630,643,656,618,631,644,657,619,632,645,658
620,633,646,659,1616,1629,1642,1655,1617,1630,1643,1656,1618
1631,1644,1657,1619,1632,1645,1658,1620,1633,1646,1659
**************************************************
** CREATING NODES AND ELEMENTS FOR THE RIGID ARM **
**************************************************
```

```
*NODE
2000,0,-28.85,-11
2010,0,-63,0
*NODE
3000,0,28.85,-11
3010,0,63,0
*NGEN, NSET=FRONT_ARM_N
2000,2010,1
*NGEN, NSET=BACK_ARM_N
3000,3010,1
*ELEMENT, TYPE=B31
2000,2000,2001
*ELGEN, ELSET=FRONT_ARM_EL
2000,10,1,1
*ELEMENT, TYPE=B31
3000,3000,3001
*ELGEN, ELSET=BACK_ARM_EL
3000,10,1,1
********************************
** MATERIAL FOR THE RIGID ARM **
********************************
*MATERIAL, NAME=RIGID_STEEL
*ELASTIC, TYPE=ISO
20000000,0.3
************************************
** BEAM SECTION FOR THE RIGID ARM **
************************************
*BEAM SECTION, ELSET=FRONT_ARM_EL, MATERIAL=RIGID_STEEL,SECTION=RECT
10,10
*BEAM SECTION, ELSET=BACK_ARM_EL, MATERIAL=RIGID_STEEL,SECTION=RECT
10,10
**************************************************************
** KINEMATIC COUPLING BETWEEN THE CLAMPS AND THE RIGID ARMS **
**************************************************************
*KINEMATIC COUPLING, REF NODE=2010
FRONT_CLAMP, 1,6
*KINEMATIC COUPLING, REF NODE=3010
BACK_CLAMP, 1,6
************************************************
** DEFINITION OF CONTACT SURFACES AND CONTACT **
************************************************
*ELSET,GENERATE,ELSET=TOP_CONT
61,540
*ELSET,GENERATE,ELSET=BOTTOM_CONT
1061,1540
*SURFACE, TYPE=ELEMENT, NAME=TOP_TAPE_SURF
TOP_CONT,SPOS
```

```
*SURFACE, TYPE=ELEMENT, NAME=BOTTOM_TAPE_SURF
BOTTOM_CONT,SNEG
*SURFACE INTERACTION, NAME=CONT
0.05,
*FRICTION
0.1,
*SURFACE BEHAVIOR, PRESSURE-OVERCLOSURE=HARD
*CONTACT PAIR, INTERACTION=CONT
BOTTOM_TAPE_SURF,TOP_TAPE_SURF
*************************
** BOUNDARY CONDITIONS **
*************************
*BOUNDARY
2010,1
2010,5
2000,1,3
2000,5,6
3010,1
3010,5
3000,1,3
3000,5,6
********************
** ANALYSIS STEPS **
********************
*STEP, INC=1000, NLGEOM
Folding
*STATIC,STABILIZE,FACTOR=0.000001
0.001, 1, 1.E-30
*BOUNDARY
2000, 4,, 1.57
3000, 4,, -1.57
*RESTART, WRITE, OVERLAY
*END STEP
****************************
****************************
*STEP, INC=1000, NLGEOM
Unfolding
*STATIC,STABILIZE,FACTOR=0.000001
0.001, 1, 1.E-30
*BOUNDARY
2000, 4,, -1.57
3000, 4,, 1.57
*RESTART, WRITE, OVERLAY
*END STEP
```